IceBridge Gravity Instrument Performance and Data Assessment

James R. Cochran[1], Stefan Elieff[2], Kirsteen J. Tinto[1] and Kevin Charles[2]

[1)]Lamont-Doherty Earth Observatory of Columbia University
61 Route 9W
Palisades, 10964
USA

[2)]Sander Geophysics Ltd,
260 Hunt Club Rd.
Ottawa, ON K1V 1C1
CANADA

Revised and corrected 25 July 2011

IceBridge Gravity Instrument Performance and Data Assessment

Contents

Introduction

Gravity measurements have been identified as a critical element of the Operation IceBridge (OIB) campaigns. Specifically, gravity field measurements to infer bathymetry beneath ice shelves and sub-ice sheet bed topography beneath outlet glaciers that cannot be mapped by radar have been identified as a critical priority. Collection of gravity data for other purposes has been identified as "desirable, but not critical". Examples of "other purposes" are improved local determination of the geoid to aid in determining sea ice freeboard in areas of sparse leads and determining bed geology and basal conditions.

We have already utilized OIB gravity data to determine the bathymetry beneath the Larsen C ice shelf and beneath Thwaites Glacier. By combining these results with the radar-determined ice thickness and laser altimetry, we were able to investigate the geometry of the water cavity. At the Larsen C ice shelf, we documented the presence of troughs that may provide warm water from the Weddell Sea access under the ice shelf [*Cochran et al.*, 2010; *Cochran and Bell*, submitted]. In the study of Thwaites Glacier, we were able to recognize a bathymetric ridge located ~ 40 km seaward of the grounding line which provided a potential stable position for the Thwaites Glacier grounding line in the past. The ice tongue is currently pinned at a peak on the ridge. We also identified a deep channel located beneath a bight in the current grounding line that marks the lowest topographic pathway to the Byrd Subglacial Basin, and is also the most likely path for future grounding line retreat [*Tinto et al.*, 2010; *Tinto and Bell*, submitted]. These results are currently being used by oceanographers to model seawater circulation under the ice and ocean water-ice interactions.

The OIB gravity data can also be used to characterize the structure and tectonics of the bed where it has been identified by radar. For example, *Block and Bell* [submitted] used OIB and previously existing gravity data (collected with the same instrumentation) to document the presence of a thick sedimentary trough beneath the main trunk of Jakobshavn Isbrae. This is significant because the presence of sediments changes the nature of the interaction between the ice and the bed and can result in increased velocity.

Collection of gravity data as part of OIB began with the 2009 Antarctic campaign, so there have been four sets of data collected with final data available for three them (Antarctica 2009, 2010, Greenland 2010) and field data for the fourth (Greenland 2011). The analysis presented here will be based on the three sets of final data.

AIRGrav gravity system

OIB gravity data is obtained using a Sander Geophysics AIRGrav airborne gravimeter (Figure 1). The AIRGrav system consists of a three-axis gyro-stabilized, Schuler-tuned inertial platform on which three orthogonal accelerometers are mounted. The primary gravity sensor is the vertical accelerometer that is held within 10 arc-seconds (0.0028 degree) of the local vertical by the Schuler-tuned inertial platform, monitored through the complex interaction of gyroscopes and two horizontal accelerometers [*Sander et al.*, 2004]. The platform design insures that the gravimeter remains vertically oriented independent of aircraft maneuvers and gives the correct scalar gravity. However, the accelerometers and gyroscopes are precise enough to also determine vector gravity components with suitable post-processing [*Argyle et al.*, 2000], raising the possibility of directly determining the local deflection of the vertical [*Ferguson*, 2010], which would be extremely valuable for sea ice
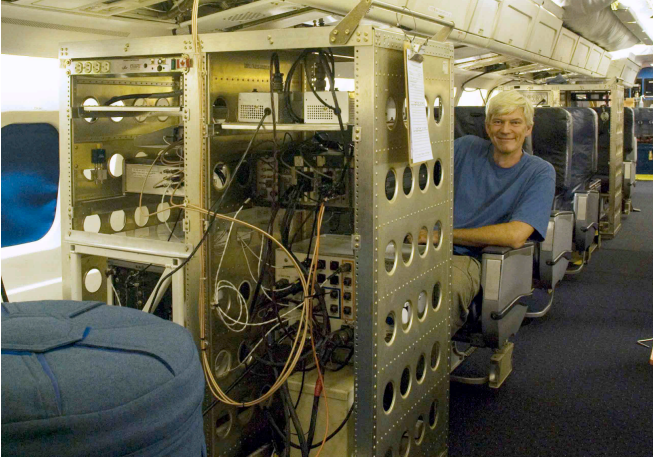
Figure 1. AIRGrav system installed on the NASA DC-8 for the Operation IceBridge 2009 Antarctic campaign.

studies.

The Sander Geophysics Limited (SGL) AIRGrav system was selected following a comparison in high latitudes of the relative performance and accuracy of an AIRGrav system with a Canadian Micro Gravity GT-1A system in side-by-side testing [*Studinger et al.*, 2008]. The GT-1A is its main competition as a gravity system specifically designed for airborne surveys.

Compared to the GT-1A system, the AIRGrav system has a lower noise level and higher accuracy and is less sensitive to changing flight conditions including, in particular, vertical accelerations during turbulent flights. Comparison of the AIRGrav system with a ground gravity data set revealed that, during that survey, the RMS difference between the ground gravity data and 4 passes of an airborne line ranged from 1.1 mGal with a 70 s filter to 0.7 mGal with a 140 s filter [*Studinger et al.*, 2008].

One great advantage of the AIRGrav system is that it is capable of collecting high quality data during draped flights [*Studinger et al.*, 2008], greatly broadening the potential applications for polar use compared to the previously used BGM-3 and LaCoste & Romberg gravimeters. Specifically, the AIRGrav system can obtain high-quality gravity data on the draped flights that are necessary to support collection of LIDAR and radar measurements as part of all of the OIB campaigns. To date, no other airborne gravity system has the demonstrated capability to collect high-resolution data during draped flight operations

Figure 2 shows two repeat free-air gravity profiles across fjords in Arctic Canada collected from a Twin Otter aircraft using the AIRGrav system. The two passes gave nearly identical gravity profiles in spite of the fact that an elevation change was necessary on one line. The anomalies over the two fjords are clearly resolved and were used to model the water depth in the fjords with an estimated accuracy of about 100 m [*Studinger et al.*, 2008]. The green dashed profile shows a simulation of the anomalies that could be recovered with a BGM3 gravimeter, which requires a much longer filter.

Positional data: Three GPS units are utilized on the aircraft to obtain positional data (time, latitude, longitude, altitude). Two additional units are used at the base of operations (Thule or Kangerlussuaq in Greenland and the Punta Arenas airport for the Antarctic campaigns) as reference stations for differential GPS processing. The GPS stations use a Novatel DL-4 integrated GPS receiver and data logger which records onto compact flash cards. The Novatel Millennium, 12-channel GPS Satellites, 12-Channel GLONASS Satellites, 2-Channel SBAS, 1-Channel L-Band multi-frequency receiver forms an integral part of the DL-4 system. It provides averaged position and raw range information of all satellites in view, sampled every 0.1 s. The comparative navigation data obtained during flights allows for post-processed differential GPS (DGPS)
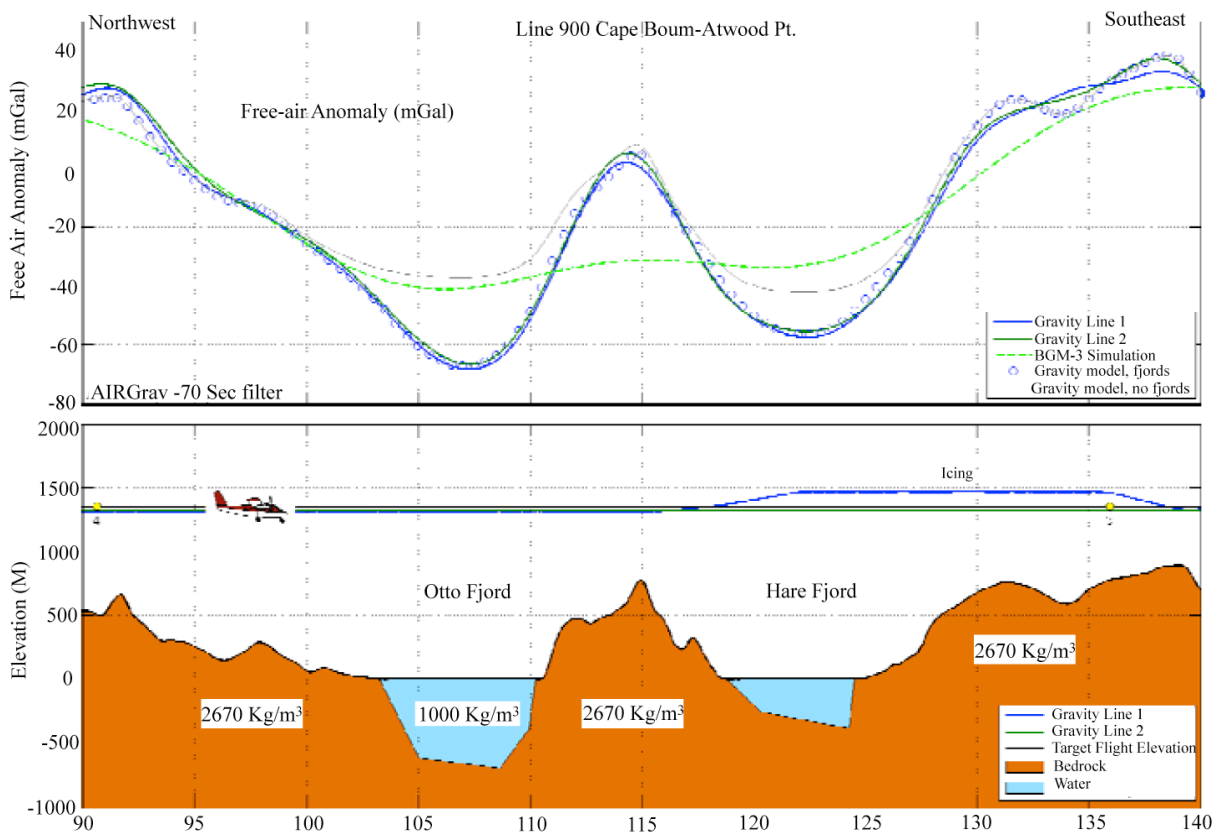
Figure 2. Repeat free-air gravity profiles across fjords on Ellesmere Island using the AIRGrav system. Green dashed line shows a simulation of anomalies that would have been recovered using BGM-3 meter. Dash-dot line shows the calculated gravity anomalies assuming the observed topographic relief and zero water depth. The AIRGrav data allows estimation of the water depth in the fjord with the resulting gravity anomalies shown as open circles Figure is from Studinger et al. [2007].

corrections for survey flights. In addition, the DGPS data is used to remove plane accelerations from the gravity signal.

Calibration and Gravity Ties

An alignment of the AIRGrav system is performed prior to each flight to ensure the proper orientation of the vertical reference. Also data is recorded on the ground prior to and after each flight to determine the consistency of the data and the drift rate. Prior to and after each flight, the AIRGrav measurements are tied to a reference gravity value adopted for the location at which the airplane is parked. The average value was used to level the data. Drift during flights rarely exceeded 1 mGal and was generally < 0.5 mGal. - At Punta Arenas, the gravity value at BGI (Bureau Gravimetric International) reference station 002163 was assumed as the ground level gravity value at the plane. This station is located in the waiting room of the old terminal building, about 70 m from where the DC-8 was parked. A free-air correction was applied to account for the height above the ground (3.25 m) of the meter in the DC-8 cabin.

- At Thule, the gravity value at BGI reference station 001801 was assumed as the ground level gravity value at the plane. This station is located in Hanger 7, at the southeast corner of the hanger; about 100 m from where the OIB planes were parked in Hanger 8. A free-air correction was applied to account for the height above the ground of the meter in the DC-8 (3.25 m) and in the P-3 (3.20 m).
- At Kangerlussuaq, the average value of four BGI reference stations (050201, 050202, 050204, 050205) at various locations at the airport was assumed as the ground level gravity value at the plane. A free-air correction was applied to account for the height above the ground (3.20 m) of the meter in the P-3 cabin.

The transfer of the gravity value from the base station to the location at which the plane is parked will add an uncertainty to the absolute level of the gravity measurements due both to the horizontal gradient in gravity and changes in elevation. Such uncertainty is relatively small (0.1-0.2 mGal) for Thule and Punta Arenas. However, the gravity reference stations used at Kangerlussuaq were distributed over a distance of about 1.5 km and vary over a range of 1.5 mGal, creating the possibility of a greater uncertainty. However, the reference value in Kangerlussuaq is tied to that in Thule by multiple ferry flights between the two bases of operation leading to confidence in the adopted value. However, it is still good practice to determine the gravity value at the plane's parking site utilizing a portable gravimeter to measure the difference in gravity between that site and nearby base stations. This will be done on future campaigns and may result in a small DC adjustment that can be easily applied to existing data sets.

The gravity data are leveled to compensate for instrument variations in two steps. A single constant shift determined from static recordings is applied on a flight-by-flight basis. The pre- and post-flight readings for each flight are averaged for each flight and the difference between the average value and the local gravity value is removed. Intersection statistics, where available, are then used to adjust individual survey lines. Intersection differences from entire lines are averaged together and a single adjustment is applied to each survey line.

Data Processing Procedures

Gravity data (raw accelerations) are recorded at 128 Hz. These accelerations are filtered and decimated to match GPS measurements (recorded at 10 Hz) using filters designed to avoid aliasing the data. During survey operations, plane accelerations may reach 0.1 G (100,000 mGal) and the data processing must extract gravity variations from this noisy environment. This is achieved by calculating the movements of the aircraft in flight by extremely accurate differential GPS measurements, which is done using proprietary SGL software. Accelerations due to gravity are determined by subtracting the GPS-determined aircraft accelerations from the inertial accelerations. The resulting accelerations are our Level 0 data product. These raw gravity measurements are then corrected for normal gravity (the expected gravity value at the measurement latitude) and the Eötvos correction and the sample interval is reduced to 2 Hz.

The following standard corrections are applied to the gravity data:

a. *Normal gravity*

$$g_{Normal} = \frac{9.7803267714(1 + 0.00193185138639 \sin^2 \Phi)}{\sqrt{1 - 0.00669437999013 \sin^2 \Phi}}$$

where Φ is the latitude of the measurement;

b. *Eötvos correction*

$$g_{E\ddot{o}tvos} = -\frac{v_x^2}{\frac{r}{(1 - e_2 \sin^2 \Phi)^{1/2}} + h} - 2W_s v_x \cos \Phi - \frac{v_y^2}{\frac{r(1 - e_2)}{(1 - e_2 \sin^2 \Phi)^{3/2}} + h}$$

where Φ is the latitude of the measurement, v_x and v_y are the aircraft velocities in the x (east) and y (north) direction, r is the Earth's radius at the equator (6,378,137 m), e_2 is a correction for the Earth's flattening toward the poles ($6.69437999013 \times 10^{-3}$), W_s is the angular velocity of the Earth's rotation ($7.2921158553 \times 10^{-5}$ rad/s), and h is the altitude of the airplane above the GRS-80 ellipsoid;

c. *Free-air correction*

$$g_{fa} = -(0.3087691 - 0.0004398 \sin^2 \Phi)h + 7.2125 * 10^{-8} h^2$$

where Φ is the latitude of the measurement and h is the altitude of the airplane above the GRS-80 ellipsoid

d. *Static correction*, g_{sc}, based on static ground recordings and repeat lines;

e. *Level correction*, g_{lc}, based on line intersections.

Thus the free-air anomaly in mGal is given as

Free-Air Anomaly = $g_{Measured} - g_{Normal} - g_{E\ddot{o}tvos} - g_{fa} - g_{sc} - g_{lc}$

where $g_{measured}$ is the measured (level 0) gravitational acceleration.

Filtering
Statistical noise in the data is reduced by applying a cosine-tapered low-pass filter to the time-series line data. The IceBridge data sets were generated with 70, 100, and 140 second full wavelength filters.

    - 70 second full wavelength filter = 0% pass at 52.5 s, 100% pass at 105 s full
    wavelength = ~ 5.2 km half-wavelength resolution at 150 m/s flying speed.
    - 100 second full wavelength filter = 0% pass at 75 s, 100% pass at 150 s full
    wavelength = ~ 7.5 km half-wavelength resolution at 150 m/s flying speed.
    - 140 second full wavelength filter = 0% pass at 105 s, 100% pass at 210 s full
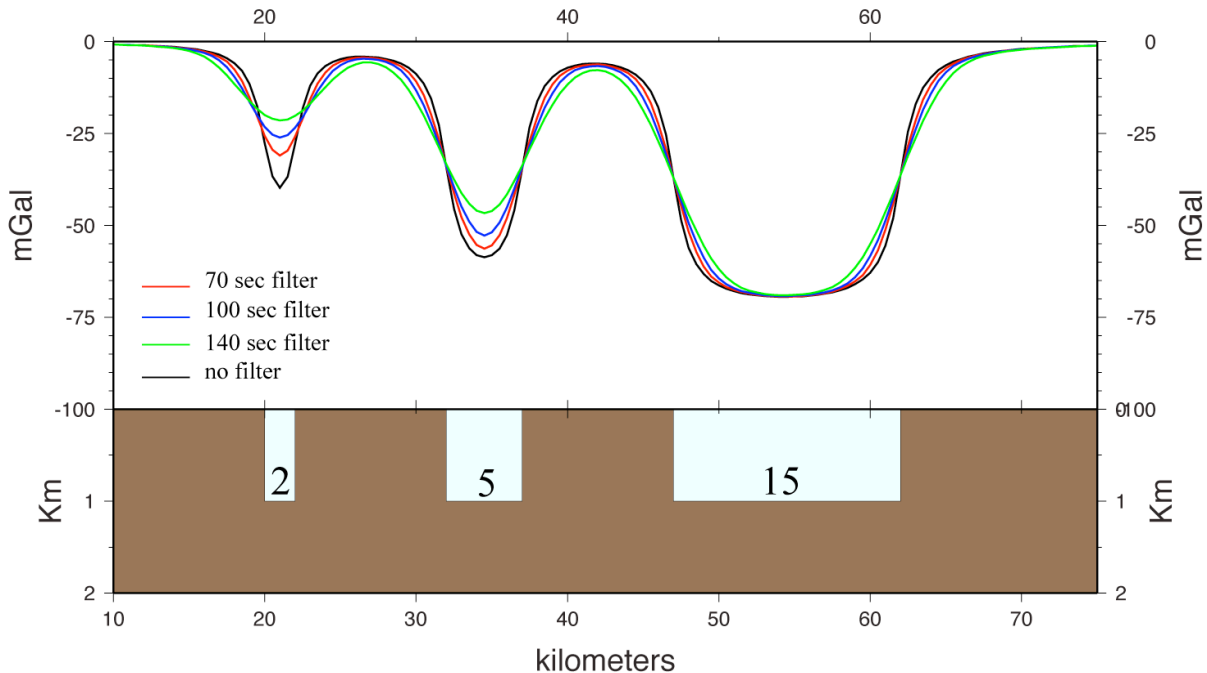   wavelength = ~ 10.5 km half-wavelength resolution at 150 m/s flying speed.

Figure 3. Gravity anomalies measured over bodies after application of different width filters. Bodies are assumed to be two-dimensional and to extend from the Earth's surface to a depth of 1 km with a density contrast of -1.80 gm/cm^3. They have widths of 2, 5 and 15 km. Black curve shows the gravity anomalies arising from these bodies at an altitude of 500 m above the surface. Red, blue and green curves show the effects of different amounts of filtering on the measured gravity at an aircraft speed of 150 m/s (~290 kts).

Figure 3 shows the effects of filtering on the gravity anomalies measured over bodies of different widths (2, 5 and 15 km) shown in light blue. The bodies are assumed to be two-dimensional and to extend from the Earth's surface to a depth of 1 km with a density contrast of -1.8 g/cm^3 with the surrounding rock. They are thus similar to fjords of different widths. The black profile shows the gravity anomalies at an elevation of 500 m above the surface, a typical height for OIB flights. The red, blue and green profiles show the anomalies observed after application of 5.2 km (70-sec), 7.5 (100 sec) and 10.5 (140 sec) cosine filters respectively. It is clear that the filter width does not represent a lower limit on the size of features that can be detected. Features with widths considerably less than the filter length can be seen, although with a reduced amplitude.

In addition to the filters described above, data within defined survey areas is gridded using a minimum curvature algorithm that averages all values within a grid cell and interpolates data between survey lines to obtain a smooth grid [*Briggs*, 1974]. Grids were generated using a 2000 m grid cell for all grids except the Russell Glacier grid, which

used a 1000 m grid cell size. Low pass filtering, directly equivalent to spatial averaging, is applied to the grid in order to reduce noise. Grid filters of various lengths, depending on the flight line density in an area, were utilized. Gravity values were extracted from the grid at original measurement points and are included as a channel in the gravity data files for lines within the gridded survey areas. These gridded values provide the most internally consistent set of data with a potentially lower noise level where the spatial averaging spans nearby lines.

Factors Affecting Gravity Resolution
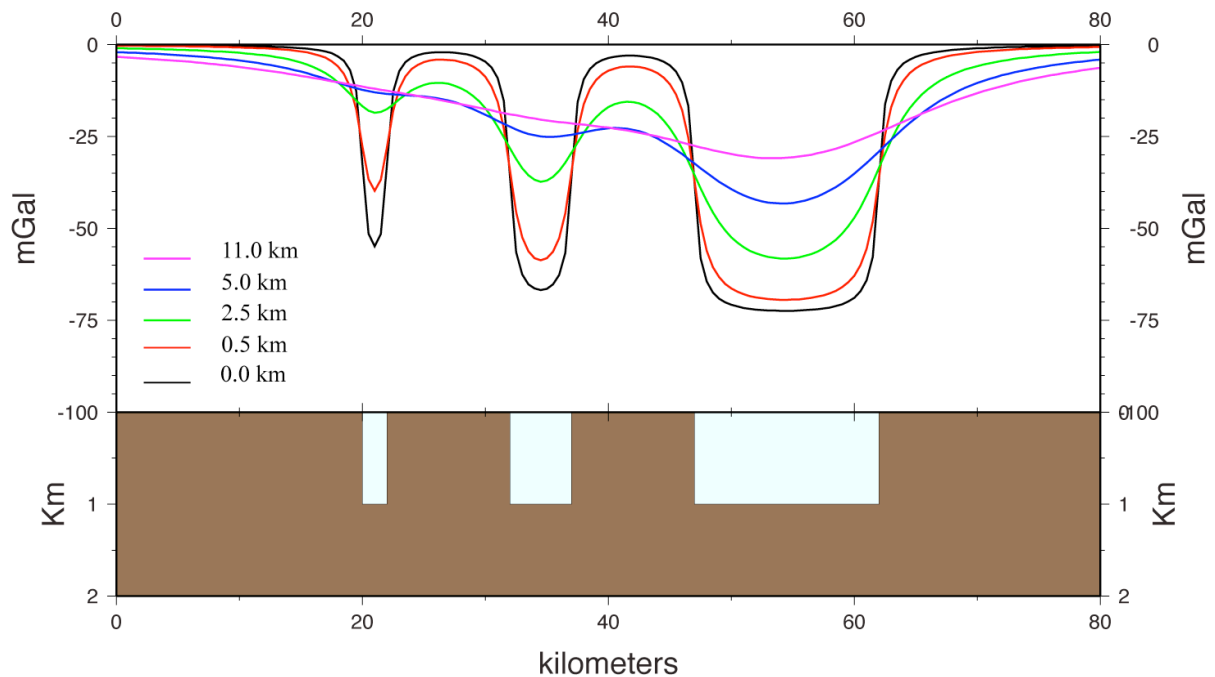
Aircraft Altitude

Figure 4. Gravity anomalies measured at different elevations above the same bodies shown in Figure 3. Bodies are assumed to be two-dimensional and to extend from the Earth's surface to a depth of 1 km with a density contrast of -1.80 gm/cm^3. They have widths of 2, 5 and 15 km.

The gravity signal decreases as 1/r, where r is the distance from the mass responsible for the gravity. Thus the amplitude of anomalies will fall off with distance above their source. Not only does the amplitude decrease, but short wavelength components are attenuated faster, so there is a loss of resolution with altitude. This is illustrated in Figure 4, which shows the gravity anomalies at a range of altitudes for the same set of model fjords shown in Figure 3. The red profile is at an elevation of 0.5 km, typical of IceBridge operations, and is identical to the "no filter" curve in Figure 3. The purple profile is at an elevation of 11 km (~36,000 feet), which is typical for LVIS operations. It can be seen that anomalies are not only attenuated but widen with elevation so that, in the 5.0 km and 11.0 km high profiles, the anomalies from our three fjords, situated 10 km apart, begin to merge together to form a composite anomaly from which it would be difficult to determine the nature of the bathymetry.
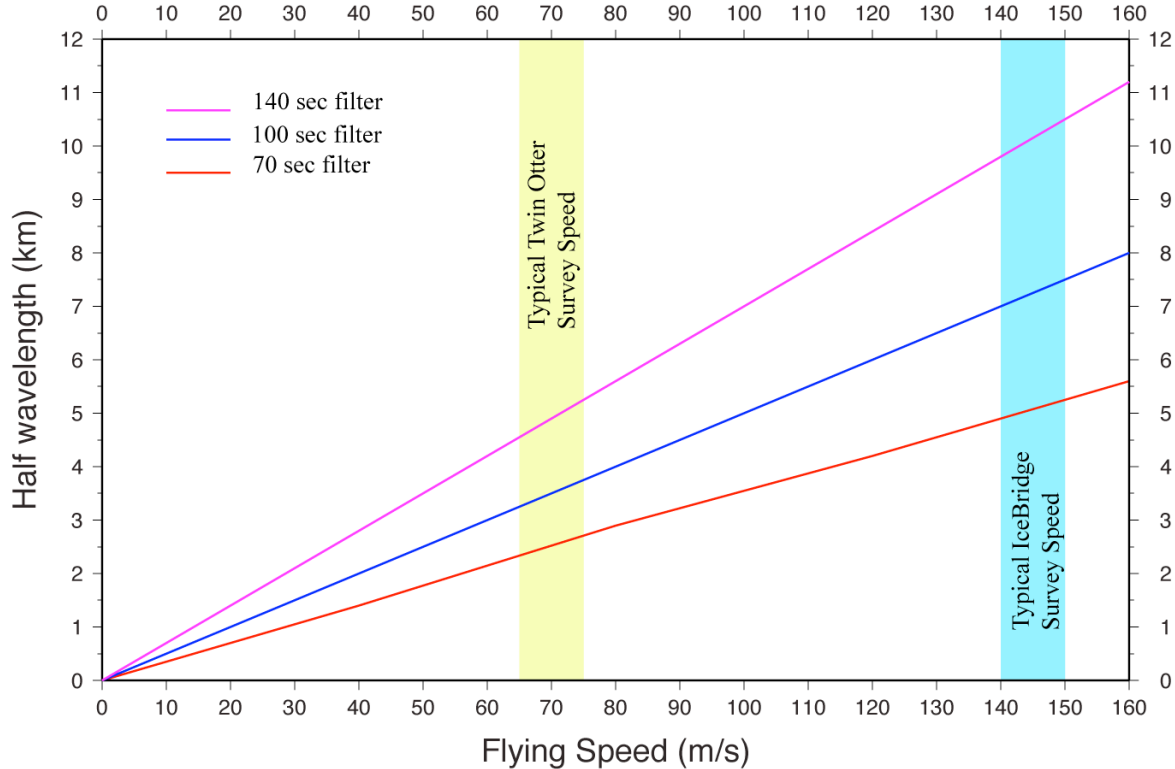
Aircraft speed

Figure 5. Variation of the spatial half-wavelength of the filter used in gravity data reduction as a function of aircraft speed. The blue band shows the typical range of survey speeds during IceBridge operations and the yellow band shows the typical speed range of Twin Otter surveys.

Gravity data reduction uses the GPS signal to compute and remove aircraft motion from the accelerations recorded by the gravimeter, leaving only the accelerations from the Earth's gravity field. The GPS signal contains noise that is time dependent, increases exponentially at shorter wavelengths and is the dominant source of error at short wavelengths. The gravity line data is low-pass filtered with time-based filters to remove this noise. The spatial length of the filter is therefore dependant on the aircraft speed. Figure 5 shows the variation in the half wavelength of the filter with flying speed for the three filters used on the IceBridge data. For typical DC-8 and P-3 operating speeds of 140-150 m/s (~270-290 knots), the filter widths for the 70 sec, 100 sec and 140 sec filters are about 5, 7, and 10 km respectively.

IceBridge flights are carried out at higher speeds than typical for airborne gravity surveys. Surveys using Twin Otter aircraft are typically flown at speeds of 65-75 m/s (~125-145 knots). At these speeds the three filters (70, 100, 140 sec) translate to spatial half-wavelengths of 2.5, 3.5, and 5 km. Thus IceBridge gravity data has a somewhat lower resolution than surveys carried out at lower speed.

Gravity Data coverage

Three categories have been defined for gravity data coverage: (a) normal data, (b) data acquired during aircraft maneuvering ("disturbed"), and (c) no data.

(a) Normal data generally means data acquired in a flight environment without excessive horizontal accelerations (essentially while flying a relatively straight line). This can include transits to and from the region of interest for a mission, climbing and descending, as well as in the area targeted for data coverage. A routine that examines horizontal accelerations uses the following procedure to identify areas with normal data coverage: The total horizontal acceleration is smoothed with a 25 second averaging filter. A threshold acceleration is set for what is considered excessive maneuvering (0.4 m/s², determined empirically from previous surveys). Data acquired during periods when the horizontal acceleration threshold is exceeded are flagged. Short isolated segments of data trapped between flagged areas are also flagged (currently segments less than 4 minutes long). An additional 30 seconds of data before/after periods of maneuvering are flagged to account for maneuver effects being spread by low pass filtering. Everything left unflagged is considered normal. Once the automated routine has been run, the results undergo quality control checks. Sometimes small manual adjustments are made, usually to add back short segments of data that were flagged but appear to be of good quality.

(b) There are cases where the gravity data may be disturbed by maneuvering but no other normal gravity data coverage exists in the area. To provide the most data coverage possible, this data may be added back as "disturbed data". The gravity signal may still contain useful information, but with either higher noise levels or by using the longer wavelength components. This is most often the case for flights paths that follow glacial flow lines or that repeat laser altimeter coverage from previous years.

(c) The remaining sections of the flight path, consisting primarily of turns between lines, have no gravity coverage. While the gravimeter itself has no settling time following turns, maneuvering effects in turns are spread by low pass filtering to data before and after turns. When gravity data is a priority, lines should be flown with lead-ins and lead-outs surrounding turns to ensure full coverage.

Identifying Gravity Coverage Type.
    The gravity data sets from each campaign are divided into lines. All survey lines are given a four-figure number starting at 1000 plus a two-figure extension after a decimal point. The flight number is included in the line number; for example lines from flight 17 all have the line number 1017.
    Each new line in a flight is denoted by an increment in the extension number. For example, 1017.04 is the 4th line detected in flight 17 with normal coverage using the procedure described above. In cases where lines are included even though they exceeded the horizontal acceleration limits ("disturbed" lines), the lines have been given extension numbers greater than 50. For example, 1017.52 is the 2nd line in flight 17 that was kept despite the aircraft maneuvering during the line. All remaining data from a flight where no line has been defined is obviously in the category of "no data" coverage.

This system has some drawbacks. Mixing line naming and data flagging together is inflexible and can be confusing. The line names are arbitrary and specific to the gravity data set. An alternate system of adding a flight environment flag channel could be used instead, such as -1 for no data, 0 for normal coverage, and +1 for disturbed data. Gravity data could then be provided by flight.

The advantage of the current scheme is that data for an area of interest is provided as a consistent data set. For example, all of the Pine Island, Thwaites, and Abbot data are grouped together and exclude high altitude data from ferry lines or LVIS flights that are located in the same geographic area. If all the data for a geographic region was extracted from a by-flight data set, care would be needed to avoid mixing data collected from vastly different altitudes.

Flight environment vs. gravity data quality

It is important to keep in mind that dividing up gravity data as described above is essentially flagging based on the flight environment, *not* data quality. Other factors, such as the quality of the GPS signal, influence the gravity data as well. Obviously there is a relationship between the flight environment and data quality when accelerations exceed the AIRGrav system's high tolerance for motion. The flagging of disturbed sections represents a simplified indicator meant to provide guidance. It is not meant to suggest the data should be discarded, but rather used with care. Some sections acquired in these conditions may be good and other sections may be usable with stronger filtering.

Aircraft Attitude Data from the Gravimeter

The gravity system produces aircraft pitch, roll, and heading information as a by-product of gravity data processing. Aircraft attitude data coverage is available and has been provided for all flights in their entirety where the gravimeter was operational. Attitude data is organized by flight instead of being divided into lines, and is at a higher 10 Hz data rate than the 2 Hz gravity data.

The accuracy of the attitude data is constrained internally since the gravity data depends on it. Some preliminary external comparisons with other systems on the aircraft using Applanix 510 and 610 data provided by LVIS and ATM have been done for a few flights. Further examination of this is planned.

Data coverage maps:

Data coverage maps are given in Figures 6-11. Black lines represent normal gravity data coverage, yellow lines are disturbed data, and red lines are no data coverage. The overall gravity coverage for the Antarctic and Arctic shown in these figures is approximately 75-80% normal data, 5% disturbed, and 10-15% no data. Please note that these maps do not include data from the 2011 Greenland campaign, which is still being processed and has not yet been divided into categories.
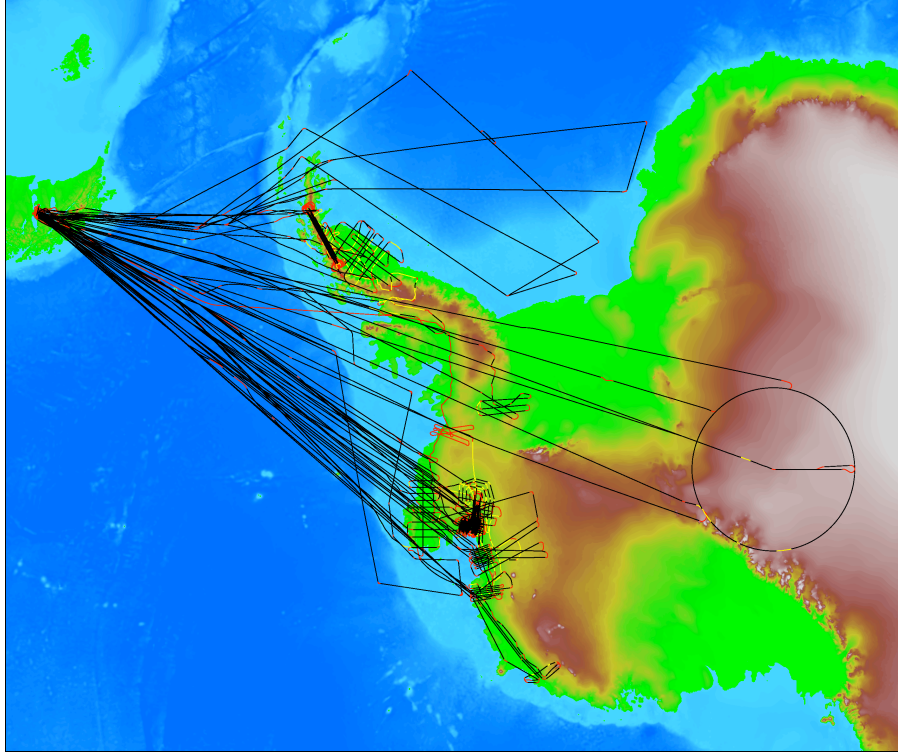
Figure 6. Antarctica gravity data coverage, 2009-2010. The flight entirely shown in red is flight 13 from 2009, which had no data due to a computer failure
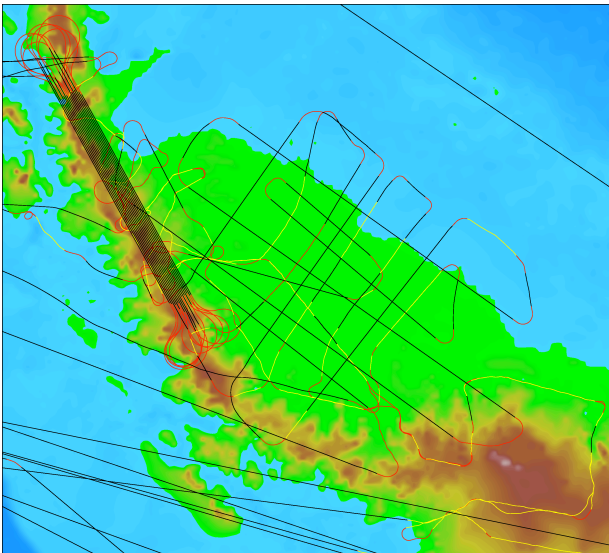

Figure 7. Gravity data in Antarctica: detailed view of the Larson and Peninsula area. Black lines show undisturbed data, yellow lines show "disturbed data" and red lines show no data areas.
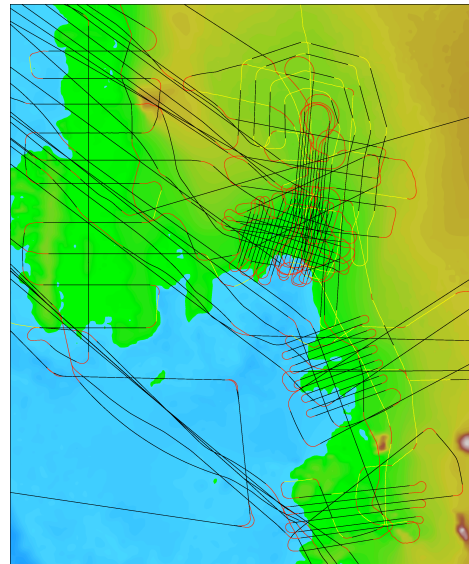

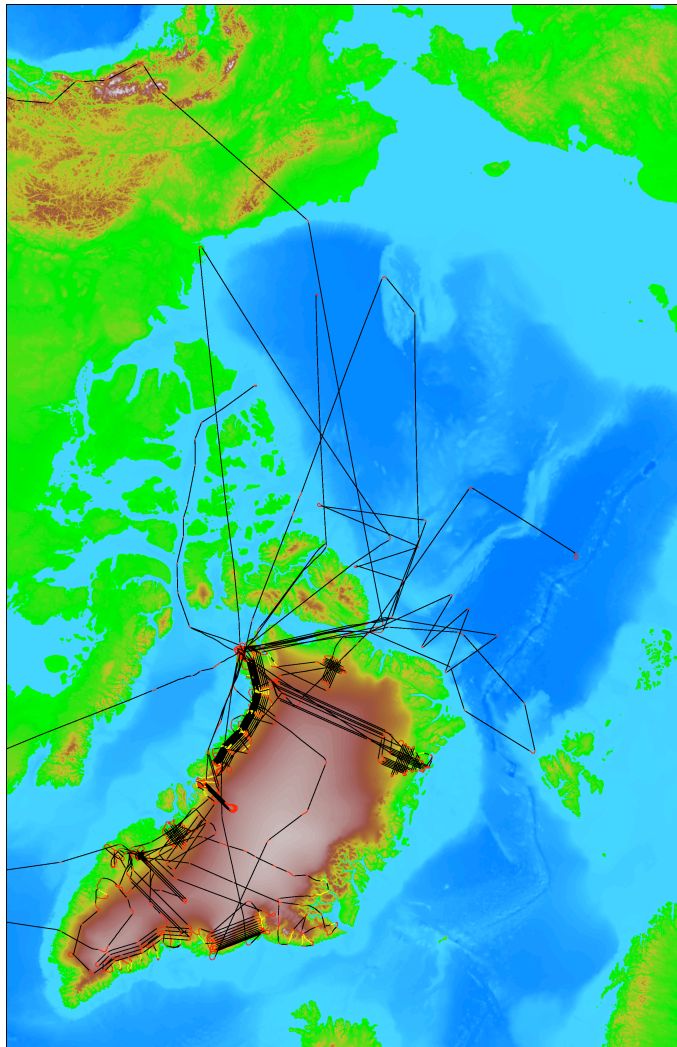*Figure 8.* Gravity data in Antarctica: detailed view of the Pine Island, Thwaites, Crosson and Abbott area. Black lines show undisturbed data, yellow lines show "disturbed data" and red lines show no data areas.

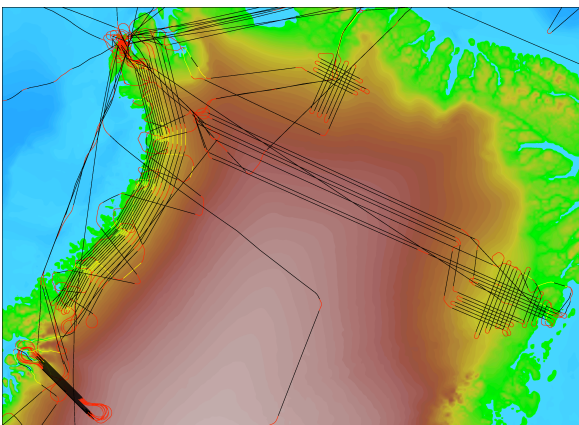*Figure 9.* Arctic gravity data coverage for the 2010 campaign.

Figure 10. Detailed view of northern Greenland coverage from 2010. Black lines show undisturbed data, yellow lines show "disturbed data" and red lines show no data areas.
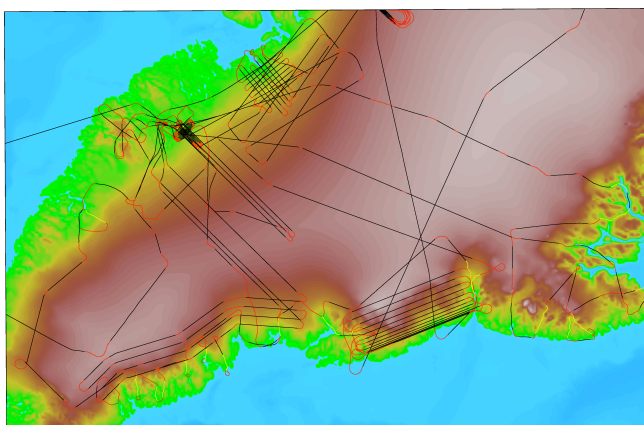

Figure 11. Detailed view of southern Greenland coverage from 2010. Black lines show undisturbed data, yellow lines show "disturbed data" and red lines show no data areas.

Accuracy and Resolution of IceBridge Gravity data

Airborne gravity accuracy assessment methods
    Two commonly used methods for assessing the quality of airborne gravity data are repeat line statistics and intersection (crossover) statistics. The two methods are similar in that they both measure internal consistency. However, intersection statistics can be strongly biased by the effect of directional filtering (caused by the different orientations of intersecting lines), which grows at longer wavelengths. In addition, both repeat lines and intersection statistics will be influenced by factors outside of instrument performance, such as comparison of data acquired at different altitudes, especially in areas with strong vertical gravity gradients. The following examples illustrate these issues to provide context for the overall IceBridge results that follow.
Intersection (Crossover) Analysis
Pine Island Glacier (Antarctica) 2009 Intersections. Several missions were flown by the DC-8 over Pine Island Glacier in 2009 creating an area with many line crossings. Figure 12 shows the intersection mismatches for the area using the 100 s full-wavelength line filtered data. The three circle sizes represent mismatches of < 2, 2 to 5, and > 5 mGal going from smallest to largest size. The gravity data here have been processed using standard gravity reduction methods (Eötvös, normal gravity field, and free air corrections). Constant shift leveling (line leveling) corrections have also been applied to some lines where there were a sufficient number of intersections for computing a correction. The leveling corrections are generally less than ±1 mGal.
    During IceBridge flights, lines are often flown to meet the requirements of a particular instrument. There are a number of lines where, in order to follow laser altimeter tracks from previous years, the aircraft was maneuvering constantly and flying zigzag ground tracks. While the AIRGrav system is highly tolerant of turbulence, height changes, and maneuvering, sufficiently aggressive maneuvering will inevitably degrade data quality. To provide as much gravity data coverage as possible a number of these lines have been retained in IceBridge data sets. This should be taken into account when an assessment is made of AIRGrav system accuracy, which is done in Figure 13. Many of the largest intersection differences have been eliminated. Bear in mind that no other existing airborne gravity instrument would be able to acquire *any* usable data under these conditions, and all other instruments would be seriously impacted at much lower maneuvering levels.
Problems related to Directional filtering. Figure 13 also gives some indication of the problem of directional filtering. A cluster of the largest remaining intersection mismatches occurs over the gravity high extending down from the top left portion of the grid toward the center. The effect of directional filtering can be simulated using gridded gravity data. A gravity grid was created from the acquired Pine Island data and filtered using a relatively short 6000 m full-wavelength grid filter, which approximates 40 seconds of filtering at 150 m/s flight speed. The grid was sampled along the line tracks. Obviously intersection differences computed on this line data sampled from the grid are 0 mGal. A 100 s line filter was then applied to data extracted along lines and intersection differences re-computed. Intersections no longer match, with the largest differences occurring around strong anomalies presenting different shapes to lines flown in different directions. This is illustrated in Figure 14, where the circles now represent intersection
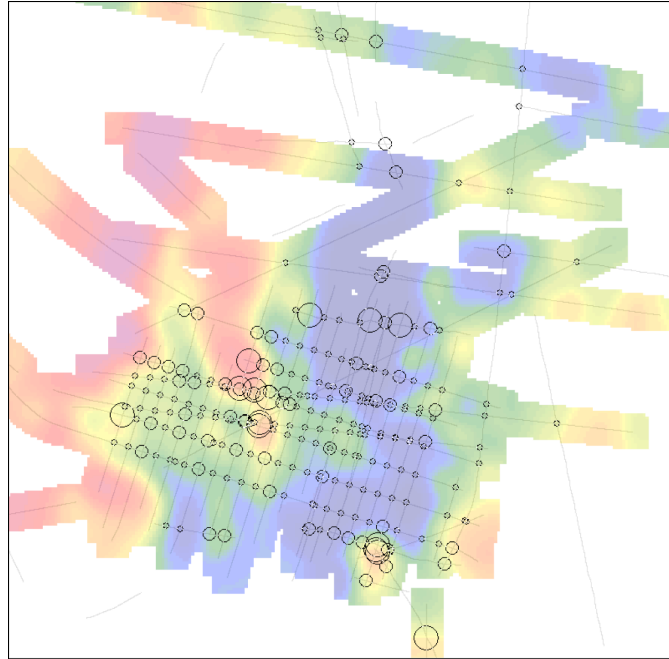
Figure 12. Intersection mismatches for 100s full-wavelength line filtered data at Pine Island Glacier with all lines included. The size of the circles is proportional to the mismatch, as discussed in the text.
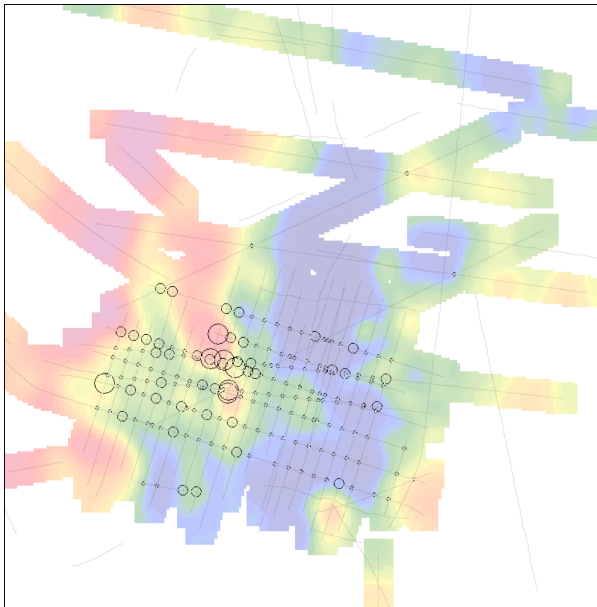

Figure 13. Intersection mismatches for 100s full-wavelength line filtered data, lines with excessive maneuvering removed. The size of the circles is proportional to the mismatch, as discussed in the text.
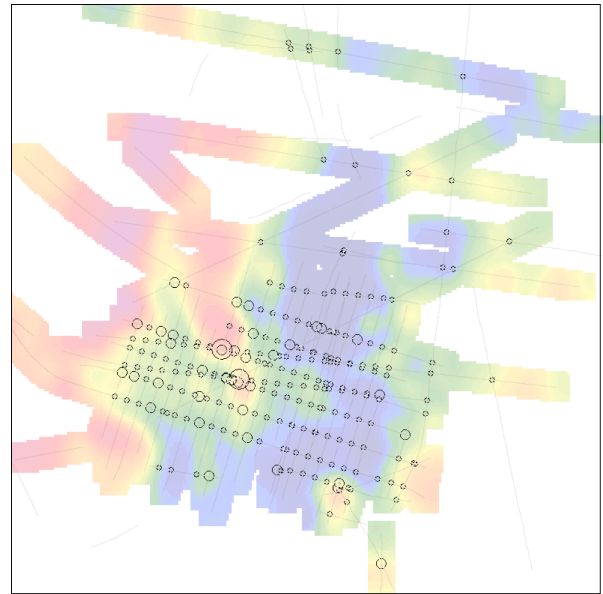

Figure 14. Simulated intersection mismatches arising entirely from the directional filtering effect for 100s full-wavelength line filtered data. Mismatches at intersections were identically zero prior to filtering. The size of the circles is proportional to the mismatch, as discussed in the text.
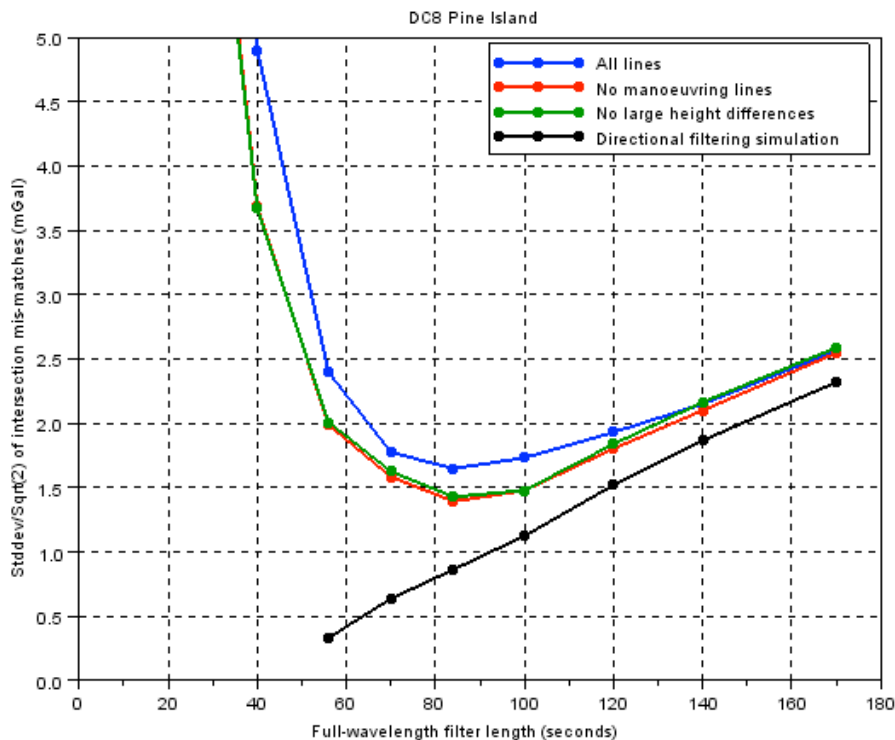
Figure 15. Intersection statistics for a range of line filter lengths for the DC-8 flights over Pine Island Glacier area. The black curve shows the mismatches resulting when applying line filters along the tracks to data points extracted from a grid with zero initial mismatch. These mismatches arise from the geometry of the anomaly field and survey lines and are independent of gravimeter performance.

differences generated as described above simulating directional filtering mismatches. Note the presence of large mismatches in the area of the same gravity high mentioned above. These mismatches are entirely due to directional filtering and are intrinsic to the geometry of the gravity anomalies and flight lines, no matter how accurately the gravity is measured.

To quantify these effects, intersection statistics were computed for line data with a range of filters applied. Results are shown in Figure 15. (Note that throughout this document, results have been divided by √2 to convert from the error on a pair of lines to the error on an individual line). In general, there is an exponential increase in intersection differences as the line filter gets shorter because the high frequency GPS noise dominates. At longer wavelengths directional filtering mismatches increase, becoming the dominant source of error and causing the curves to turn back upwards.

The magnitude of mismatches decreases when switching from using all lines (blue curve) to a subset where lines with excessive maneuvering are removed (red curve). Also plotted are intersections with large (greater than +/- 30 m) flying height differences removed (green curve). In the case of Pine Island, these had little impact on the overall statistics. The black line shows the simulated intersection mismatches for progressively longer line filters caused by directional filtering created using the procedure described
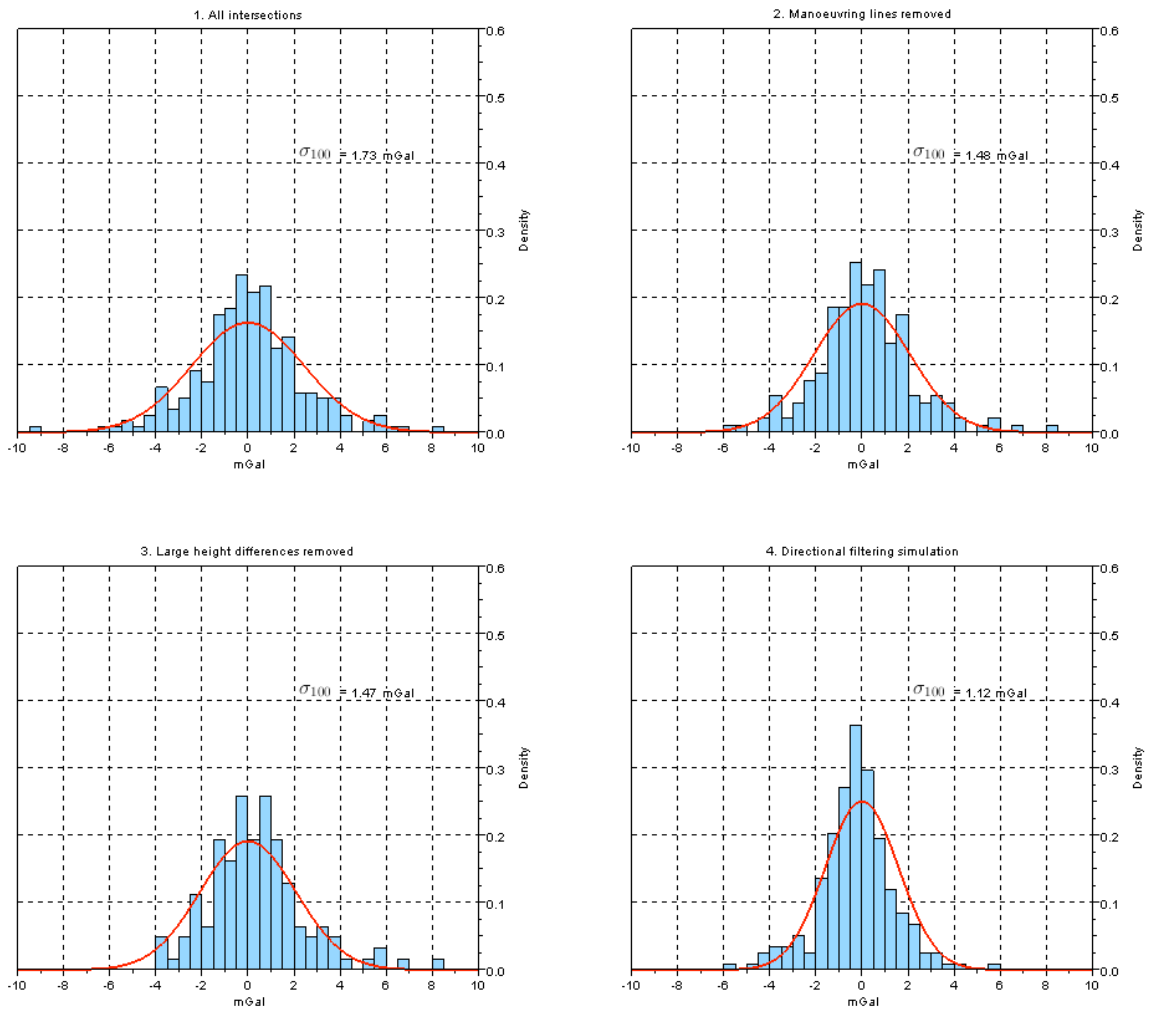
Figure 16. Pine Island intersection differences for a 100 s filter using all lines (top left), with excessive maneuvering lines removed (top right), with large height differences removed (bottom left), and for the simulated directional filtering mismatches (bottom right)

above. Mismatches arising from directional filtering effects clearly make up a significant portion of intersection mismatches for the Pine Island area.

Figure 16 shows histograms of intersection differences for the 100 s filter using all lines (top left), with excessive maneuvering lines removed (top right), with large height differences removed (bottom left), and for the simulated directional filtering mismatches (bottom right). With the histogram it is possible to see that removing intersections with large height differences did remove a few of the largest outliers (compare top right to bottom left histogram) even though the overall statistics changed very little. The error due to directional filtering for the lines run at PIG during the 2009 Antarctic campaign when the data is gridded to give 0 mGal unfiltered mismatches at intersections is 1.12 mGal. This makes up most of the 1.47 mGal error calculated for the actual data (Figure 15, 16).
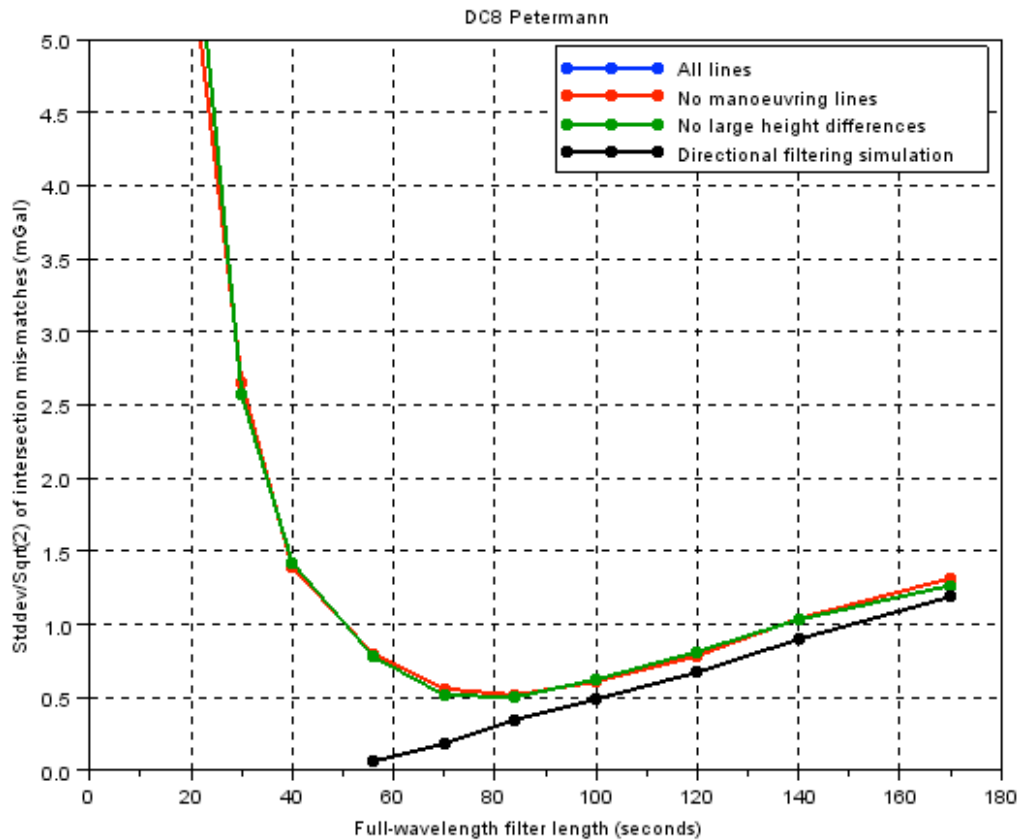
Figure 17. Intersection statistics for a range of line filters for DC-8 flights over Petermann Glacier area in Greenland. Note that in this particular case the blue (all lines) and red (no excessive maneuvering) curves are identical, so the blue curve cannot be seen. The black curve shows the mismatches resulting when applying line filters along the tracks to data points extracted from a grid with zero initial mismatch. These mismatches arise from the geometry of the anomaly field and survey lines and are independent of gravimeter performance.

Petermann Glacier (Greenland) 2010 Intersections: To contrast with the results for Pine Island glacier, the intersection statistics were also computed for the Petermann Glacier area of Greenland flown with the DC-8 in 2010. There were no excessive maneuvering lines in the area and the geological signal was relatively subdued, reducing directional filtering effects. Using a 100 s line filter, the error level is 0.62 mGal. Almost all of the mismatch can be attributed to the effects of directional filtering as shown in Figure 17.

Repeat Line Analysis
DC-8 sea ice 2009-2010 repeat lines: A better indication of system performance can be provided by repeat lines. The DC-8 flew sea ice lines in 2009 that were repeated in 2010. These lines were flown within the normal flight envelope of the AIRGrav system and are free from the complications presented by directional filtering. Figures 18, 19, and 20 show profiles of the three repeated lines and histograms of the differences. The noise levels calculated from the standard deviations are 0.48, 0.79, and 0.49 mGal. The DC-8 also flew a repeat line during a single flight during the 2010 Greenland deployment. This
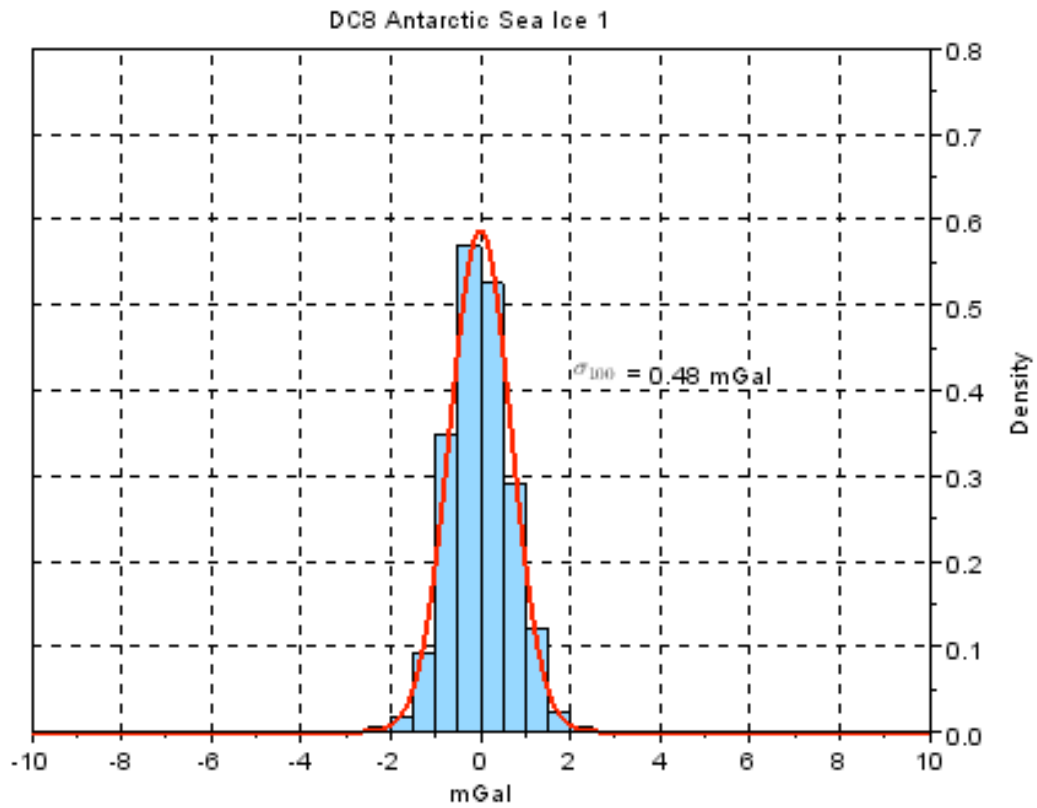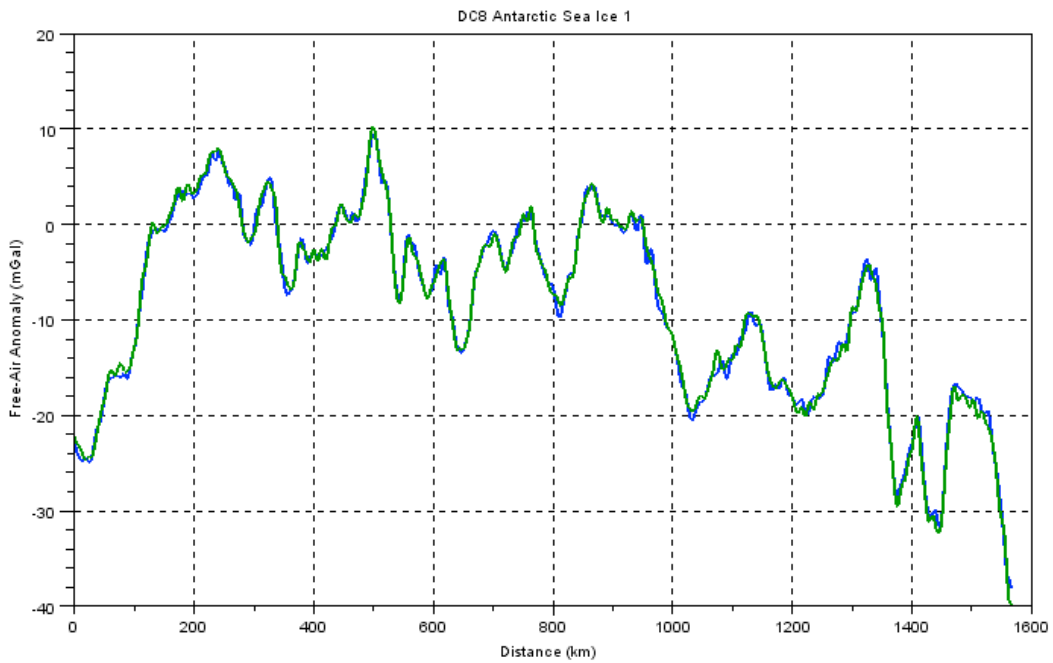
-17-

Figure 18. DC-8 Antarctic Sea Ice repeat line 1. Upper panel superimposes the two lines and the lower panel shows the distribution of mismatches. The noise level calculated from the standard deviation is 0.48 mGal.
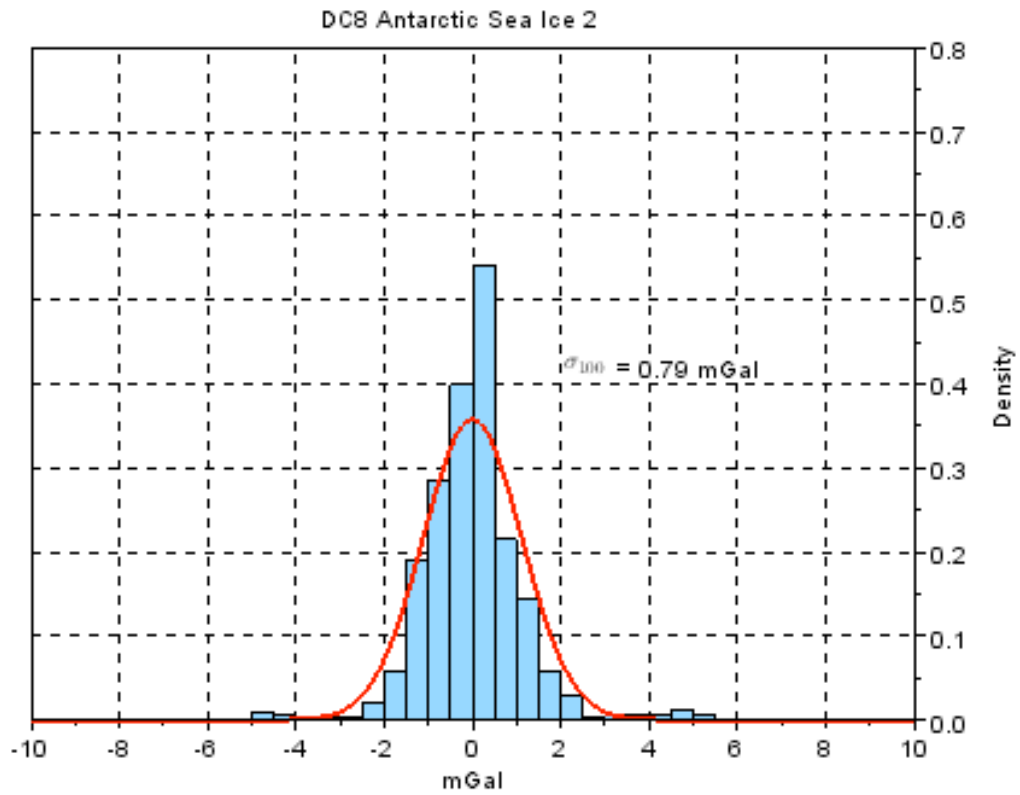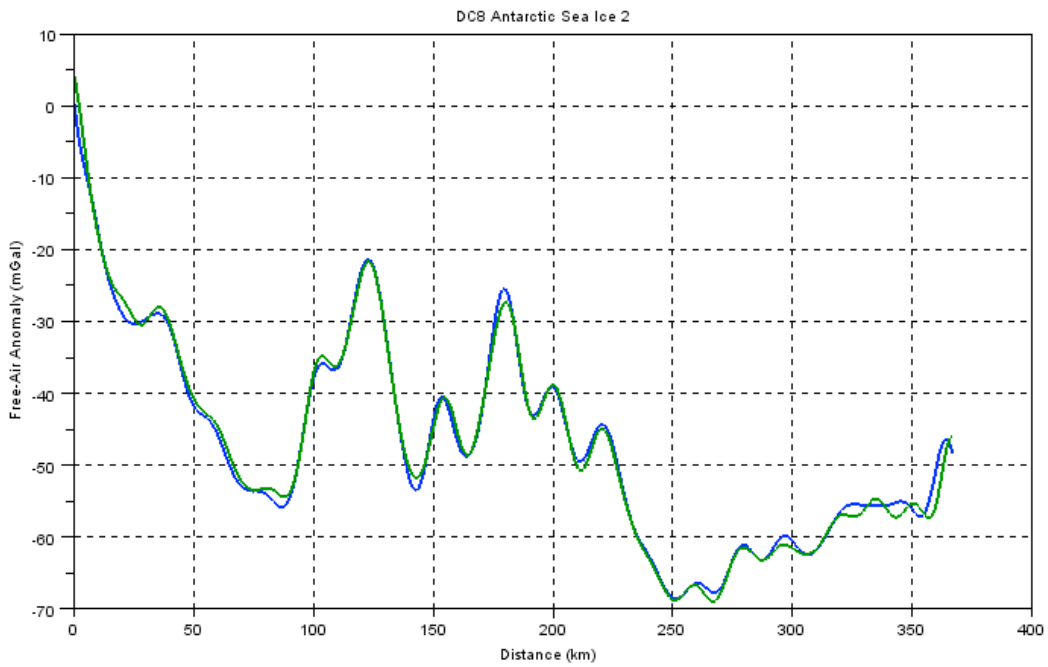
Figure 19. DC-8 Antarctic Sea Ice repeat line 2. Upper panel superimposes the two lines and the lower panel shows the distribution of mismatches. The noise level calculated from the standard deviation is 0.79 mGal.

Figure 20. DC-8 Antarctic Sea Ice repeat line 2. Upper panel superimposes the two lines and the lower panel shows the distribution of mismatches. The noise level calculated from the standard deviation is 0.49 mGal.
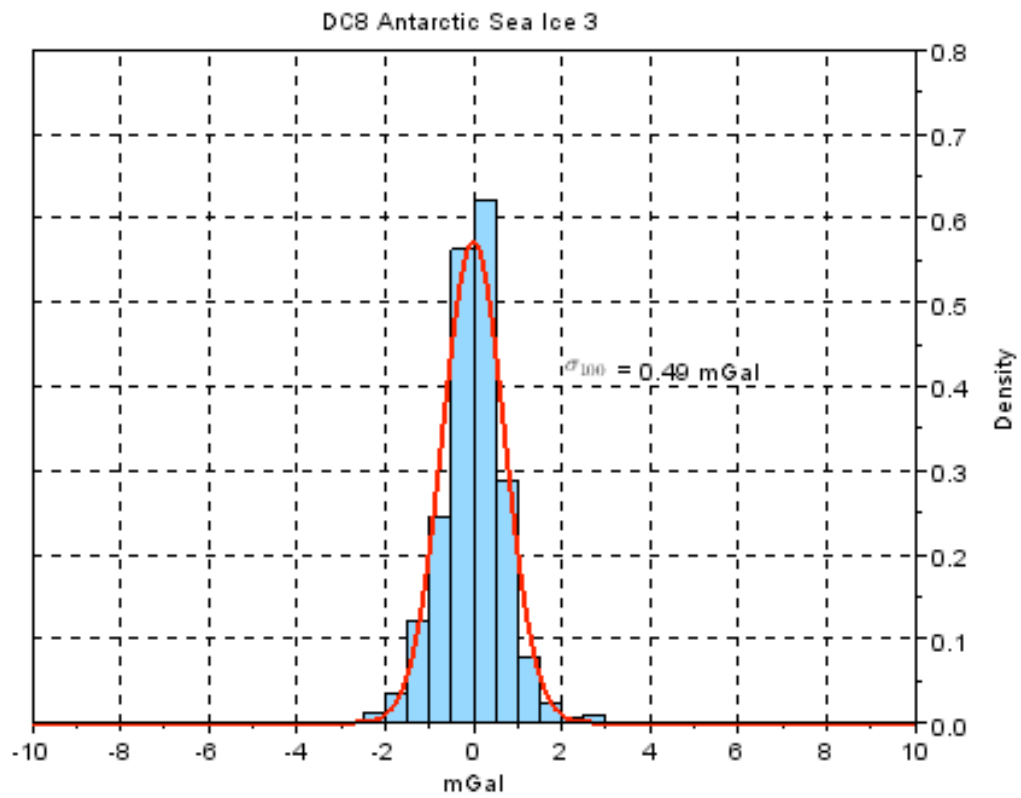
Figure 21. DC-8 Arctic Sea Ice repeat line. Upper panel superimposes the two lines and the lower panel shows the distribution of mismatches. The noise level calculated from the standard deviation is 0.30 mGal.
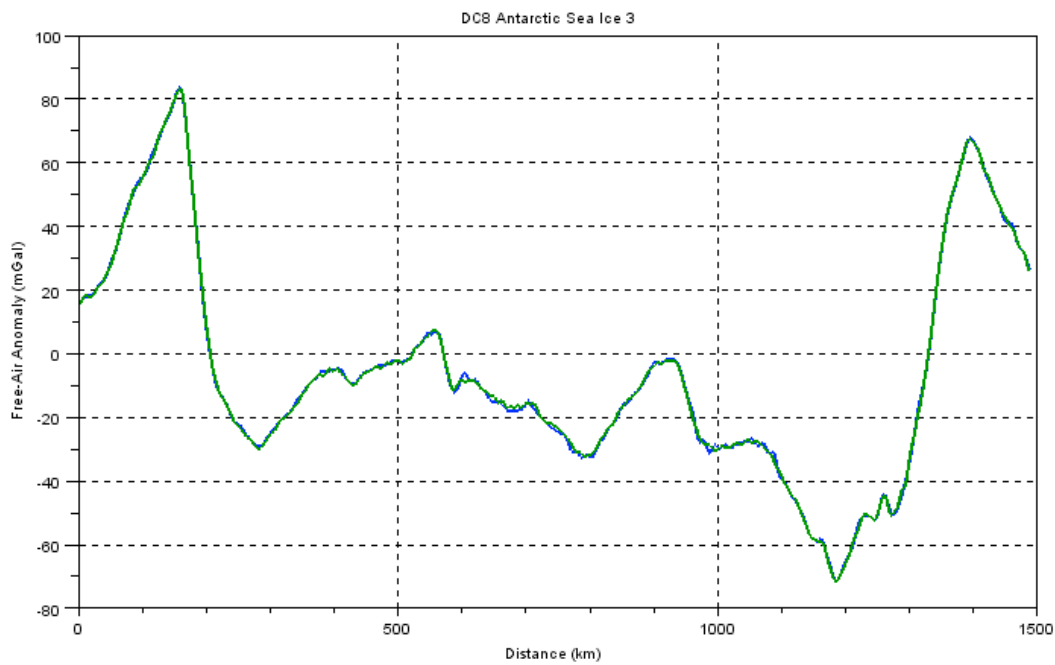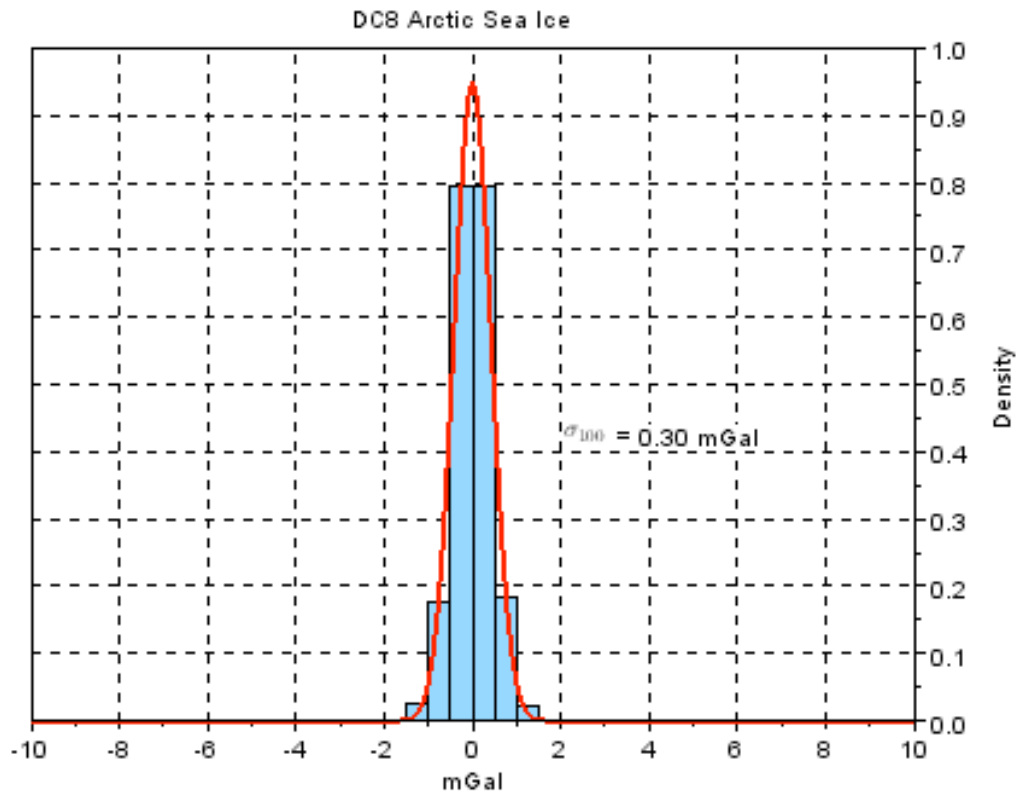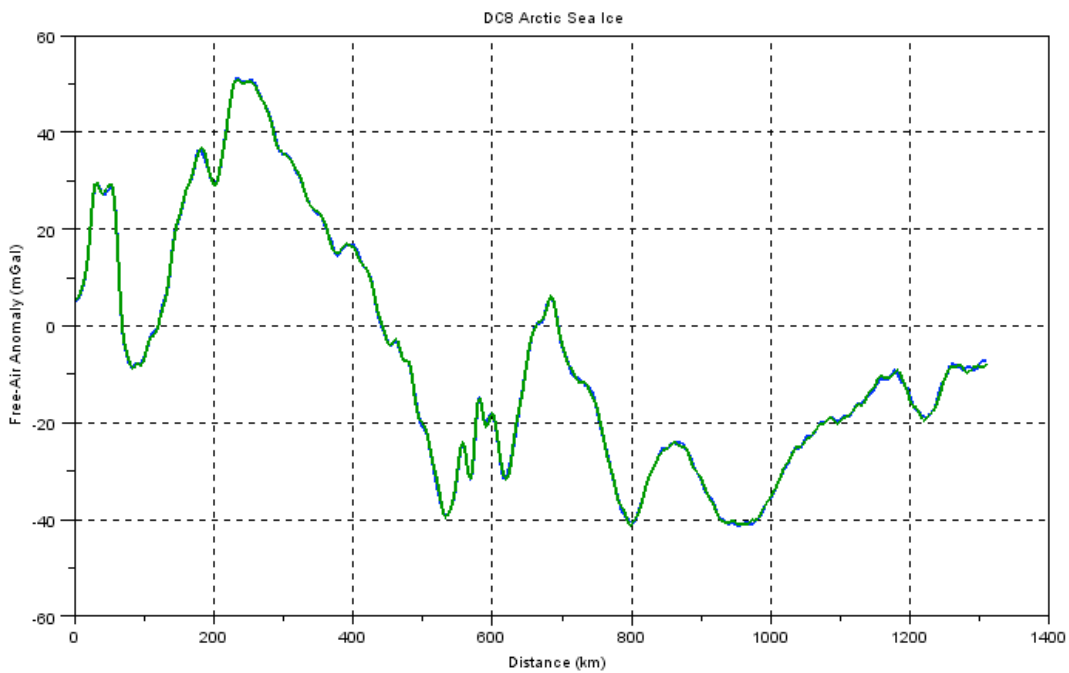
is shown in Figure 21 and the noise level was 0.30 mGal. The 100 s line filter is used in all examples. Constant offsets between the passes, which like leveling corrections are typically less than ± 1 mGal, have been removed in the figures. *P-3 2010 repeat lines.* During May, 2010, the P-3 reoccupied a line from Thule to Camp Century 5 times during 4 different flights. These repeat lines can be used to evaluate AIRGrav performance in the P-3 and the gravity line and statistics are
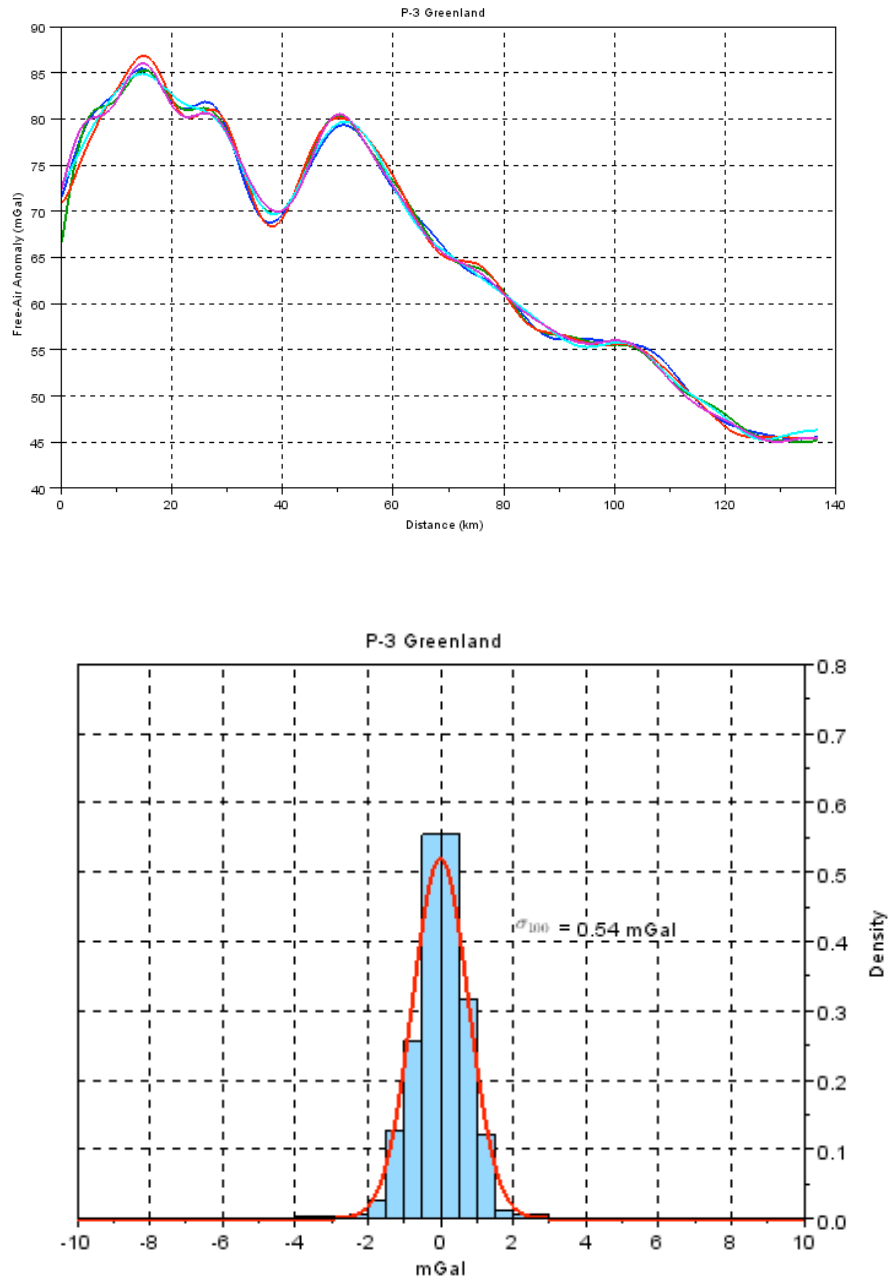

Figure 22. P-3 repeat lines between Thule and Camp Century. Upper panel superimposes the five lines and the lower panel shows the distribution of mismatches. The noise level calculated from the standard deviation is 0.54 mGal.

plotted in Figure 22. The noise level computed from the repeat lines is 0.54 mGal using a 100 s filter, similar to the results for the AIRGrav system in the P-3.

The examples shown above of individual repeat lines all gave similar results with a noise level in the range of 0.30 mGal to 0.79 mGal. However analysis of crossovers within grid surveys gave a wider distribution of mismatches at intersections that can be duplicated by simulated directional filtering of zero mismatch data. Clearly, there are difficulties arising from the effects of directional filtering with using crossovers as the primary evaluation of data quality for airborne gravity data. Directional filtering results in mismatches at line intersections that are a function of the amplitude, wavelength and geometry of the local gravity anomalies and the geometry of the survey flight lines and are not related to the performance of the gravimeter. Analyzing repeat lines or intersections from areas where directional effects are small is necessary for an accurate measure of system performance.

Airborne Gravity Accuracy Assessment: Antarctica 2009-2010, Greenland 2009

The entire IceBridge gravity data set available up to the end of 2010 was searched to identify all intersections and all repeat line segments. Differences were computed for the three sets of line filters used in gravity data sets: 70s, 100s, and 140s full-wavelength. Histograms of the differences have been generated for the 100s data, with standard deviations for all three filter lengths noted on the plots. As before, results are divided by $\sqrt{2}$ to convert from the error on a pair of lines to the error on an individual line.

Repeat Line Segments
Repeat line segments were identified by an automated search routine that found pairs of line segments which were within 500m horizontally and lasted a minimum of 10 minutes. Comparisons between line segment pairs were restricted to sections flown within 200m horizontally and 500m in altitude. The figures below show the results from all available repeat gravity data (figure 23), "normal" gravity data only (figure 24), and data acquired during high horizontal accelerations only (figure 25).

As shown in the gravity coverage maps earlier, the vast majority of gravity data acquired is in normal conditions. This is due in part to the nature of flights (long straight ferries in Antarctica, long sea ice lines, and a number of areas covered by grids of straight lines) and in part because "normal" for the AIRGrav system covers a wide range of flight conditions up to a considerable amount of maneuvering. The same is true for repeat line segments. While over 27 hours of repeat line data was identified where both lines were flown in normal conditions, only 0.3 hours of gravity data were available where both lines met the definition for high maneuvering.
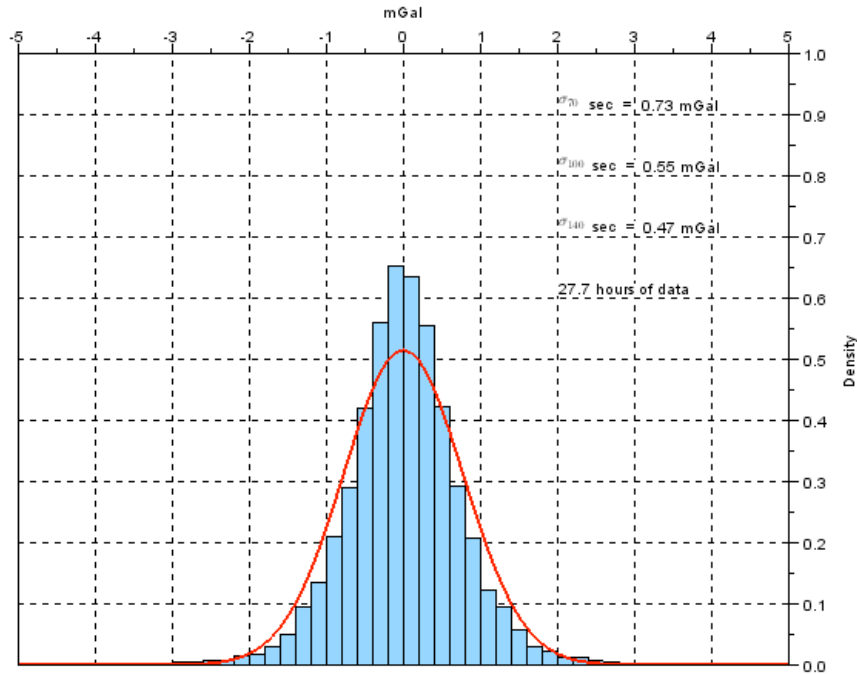
Figure 23. Distribution of gravity differences on all Operation IceBridge repeat line segments. The noise level calculated from the standard deviation of the differences is 0.73 mGal for a 70-sec full-wavelength filter, 0.55 mGal for a 100-sec full-wavelength filter and 0.47 mGal for a 140 sec full-wavelength filter.
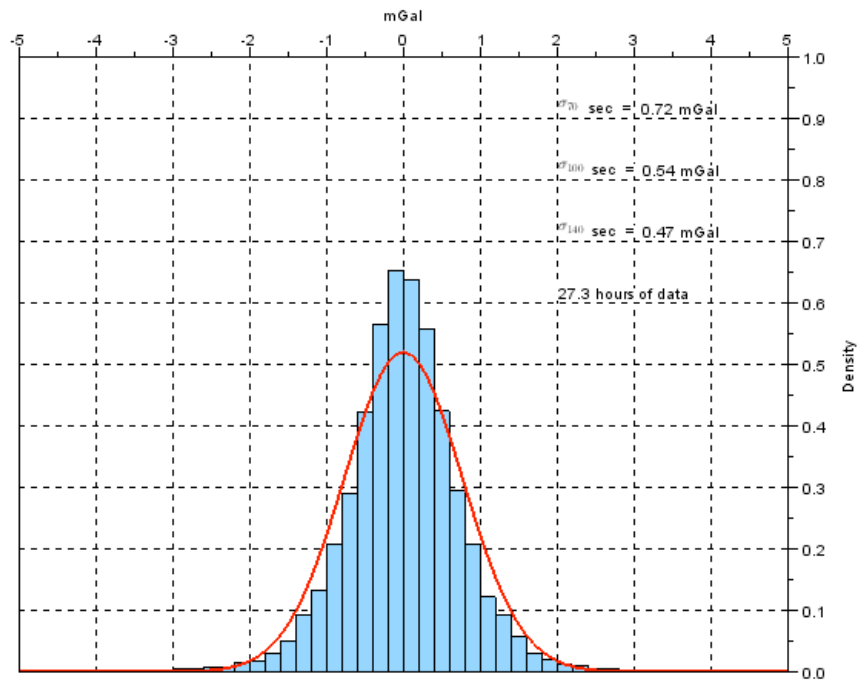

Figure 24. Distribution of gravity differences on Operation IceBridge repeat line segments collected under normal operating conditions. The noise level calculated from the standard deviation of the differences is 0.72 mGal for a 70-sec full-wavelength filter, 0.54 mGal for a 100-sec full-wavelength filter and 0.47 mGal for a 140 sec full-wavelength filter.
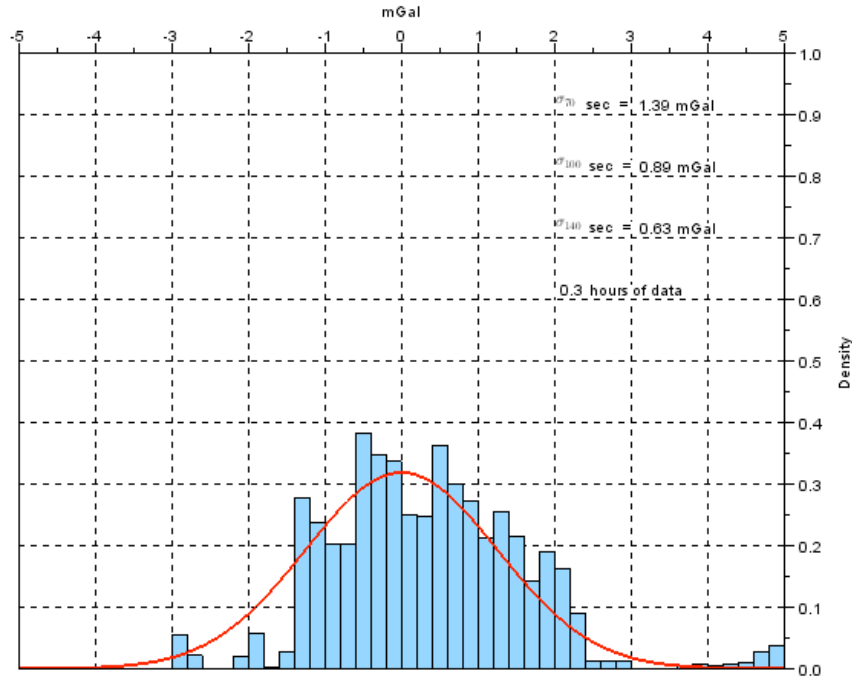
Figure 25. Distribution of gravity differences on Operation IceBridge repeat line segments collected under disturbed operating conditions. The noise level calculated from the standard deviation of the differences is 1.39 mGal for a 70-sec full-wavelength filter, 0.89 mGal for a 100-sec full-wavelength filter and 0.63 mGal for a 140 sec full-wavelength filter.

Repeat line data in normal conditions for the entire data set is in general agreement with the smaller subsets of data presented earlier. The standard deviation of differences is 0.72 mGal at 70s full-wavelength, 0.54 mGal at 100s full-wavelength, and 0.47 mGal at 140s full-wavelength.

The results obtained during maneuvering should be viewed with caution since it is relatively small amount of data. Keeping that in mind, the standard deviation increased to 1.39 mGal at 70s full-wavelength, 0.89 mGal at 100s full-wavelength, and 0.63 mGal at 140s full-wavelength. Note that the relative increase in noise level decreases at longer wavelengths, and the results at 140s with maneuvering are similar those at 70s and 100s in normal conditions. This suggests accuracy can be maintained, at the cost of reduced resolution, by using the stronger low pass filter on lines with maneuvering.

Figures 26 and 27 show the results individually for the Arctic 2010 and Antarctic 2009-2010 gravity data sets acquired in normal conditions. Noise levels calculated for these two subsets of the data are nearly identical to each other and to the complete data set.
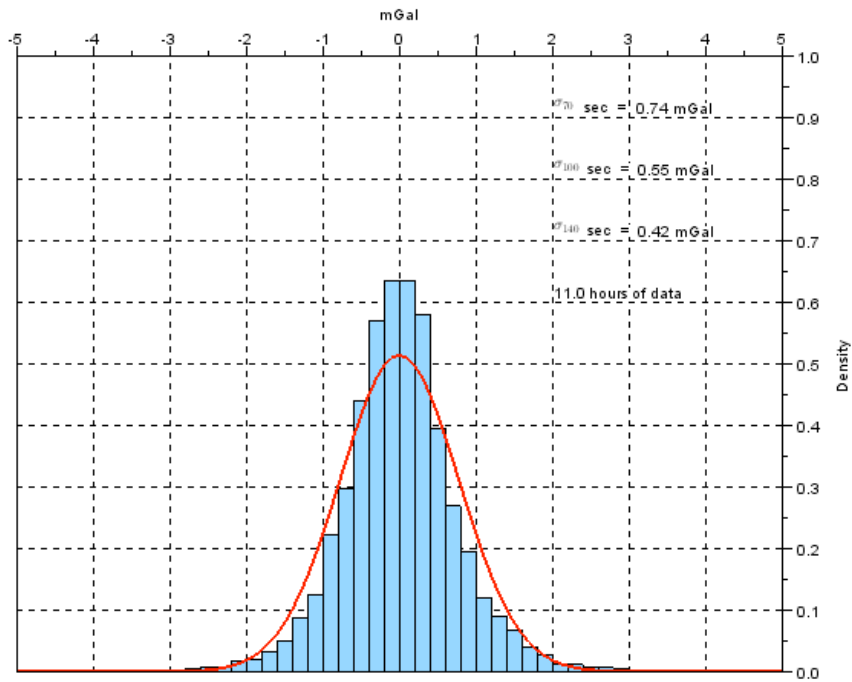
Figure 26. Distribution of gravity differences on Operation IceBridge repeat line segments collected under normal operating conditions in the Arctic. The noise level calculated from the standard deviation of the differences is 0.74 mGal for a 70-sec full-wavelength filter, 0.55 mGal for a 100-sec full-wavelength filter and 0.42 mGal for a 140 sec full-wavelength filter.
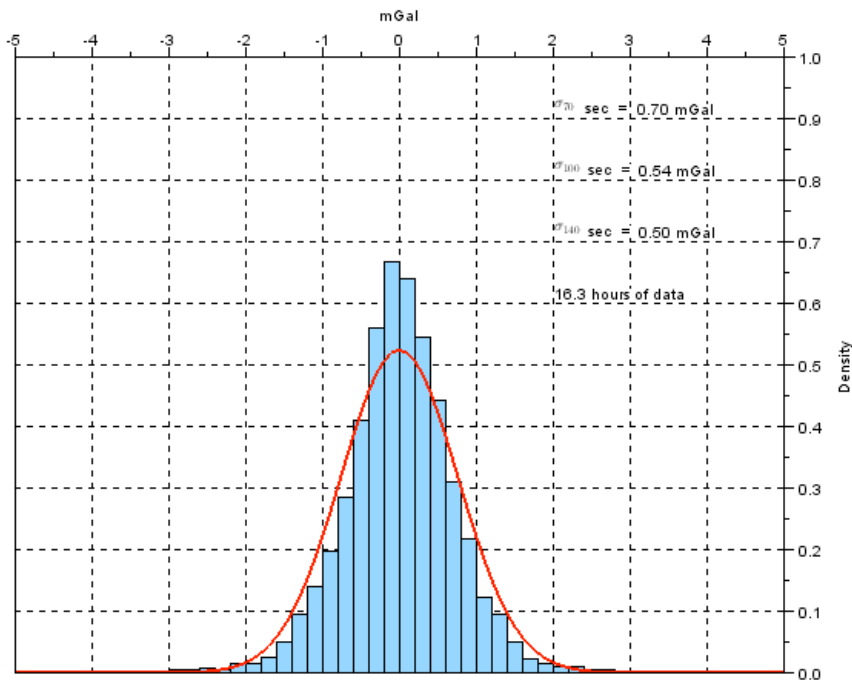

Figure 27. Distribution of gravity differences on Operation IceBridge repeat line segments collected under normal operating conditions in the Antarctic. The noise level calculated from the standard deviation of the differences is 0.70 mGal for a 70-sec full-wavelength filter, 0.54 mGal for a 100-sec full-wavelength filter and 0.50 mGal for a 140 sec full-wavelength filter.

Flight path intersections were identified using an automated search routine, then limited to those within 100 m in altitude. 568 intersections were located in the Arctic and 386 in the Antarctic. As expected, intersection statistics have a much wider spread than do repeat line segments as a result of directional filtering of the geological signal. Figures 28 and 29 show Arctic and Antarctic intersection differences analogous to those for repeat line segments given in Figures 26 and 27. The results from the Arctic show particularly strong directional filtering effects, as a result of the extensive amounts of data collected over areas such as Jakobshavn Isbrae, which has a strong, linear gravity anomaly with flight lines flown either parallel or perpendicular to it. The differences increase with stronger low pass filtering, also an indication that directional filtering effects dominate in this type of analysis. Figures 30 and 31 give an overview of the location of Arctic and Antarctic intersections used in the histograms.

Figure 28. Distribution of gravity differences at Operation IceBridge track intersections for data collected under normal operating conditions in the Arctic. The noise level calculated from the standard deviation of the differences is 2.25 mGal for a 70-sec full-wavelength filter, 2.88 mGal for a 100-sec full-wavelength filter and 3.56 mGal for a 140 sec full-wavelength filter.
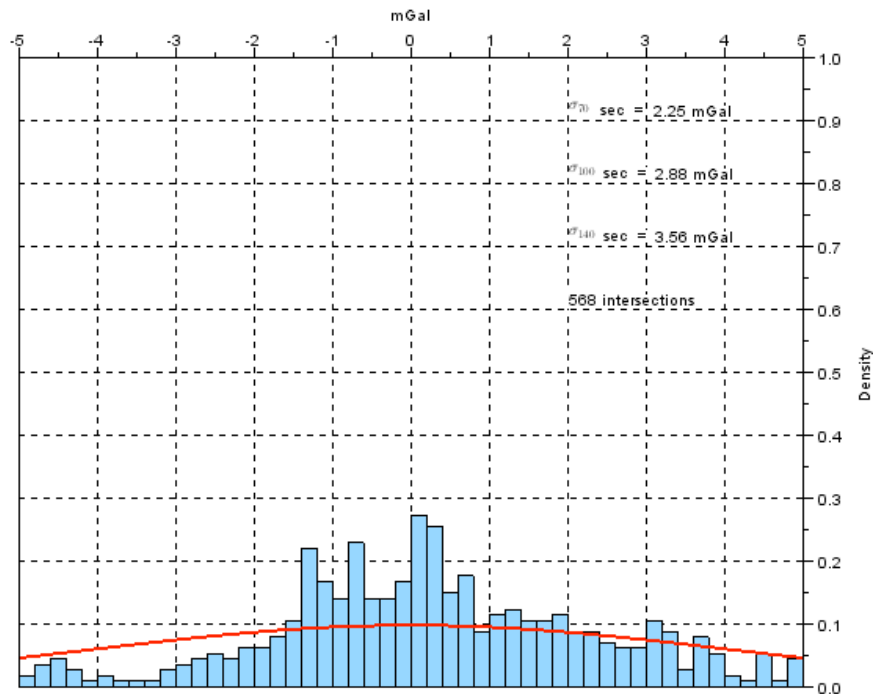
Figure 29. Distribution of gravity differences at Operation IceBridge track intersections for data collected under normal operating conditions in the Antarctic. The noise level calculated from the standard deviation of the differences is 1.03 mGal for a 70-sec full-wavelength filter, 1.22 mGal for a 100-sec full-wavelength filter and 1.80 mGal for a 140 sec full-wavelength filter.
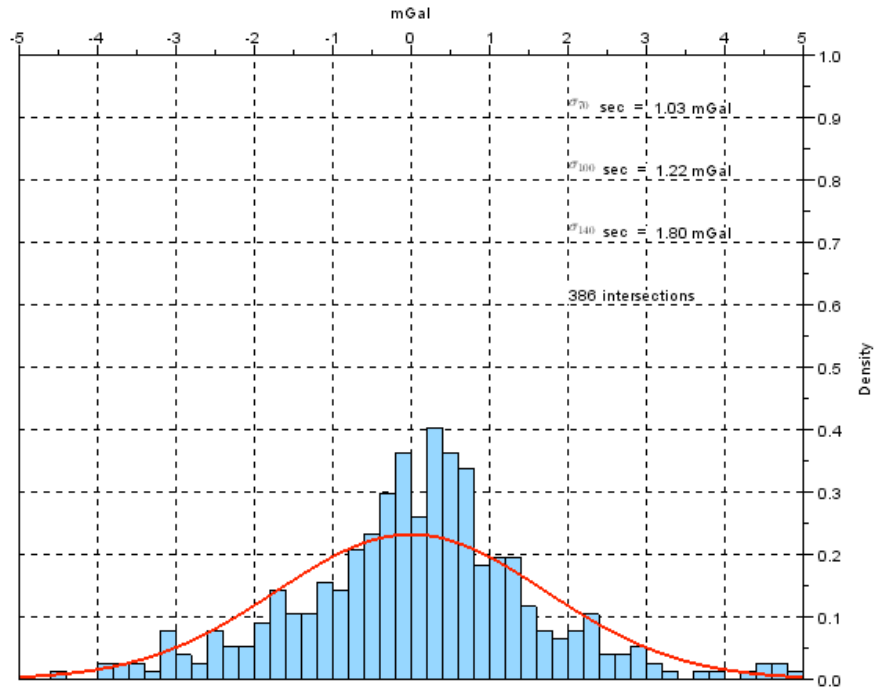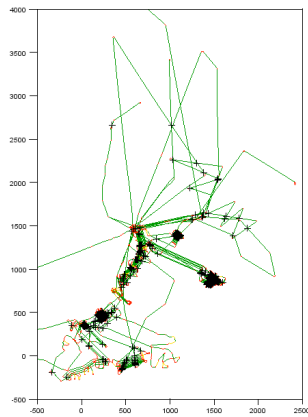

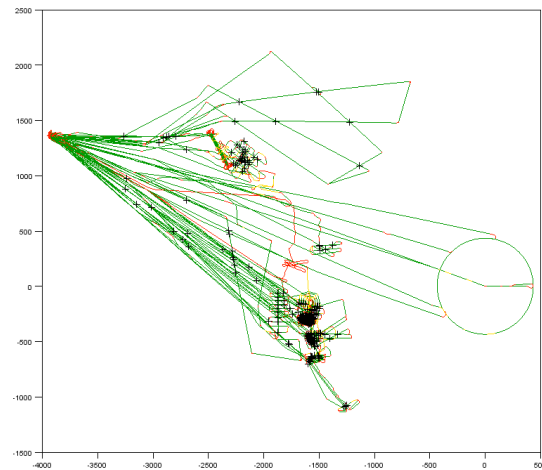*Figure 30.* Location of intersections used to generate the Arctic intersection differences.

Figure 31. Location of intersections used to generate the Antarctic intersection differences.

Uncertainties in Higher-Order (Derived) Products

The primary role of gravity measurements within OIB is "to infer bathymetry beneath ice shelves and sub-ice sheet bed topography beneath outlet glaciers that cannot be mapped by radar". The interpretation of the gravity anomalies in terms of sub-ice bathymetry and topography is also subject to uncertainties and resolution limits, which we will examine in this section. We have used IceBridge data to investigate the geometry of the water-filled cavity beneath floating ice in two very different settings, large ice shelves [*Cochran et al.*, 2010; *Cochran and Bell*, submitted] and individual glaciers [*Tinto et al.*, 2010; *Tinto and Bell*, submitted]. These two settings call for very different interpretation techniques and thus potentially different uncertainties.

Bathymetry beneath floating ice shelves
Floating ice shelves border much of the Antarctic Peninsula as well as the coasts facing the Bellingshausen and Amundsen Seas. Over the past 50 years many of the more northerly ice shelves have retreated or broken up [e.g., *Doake and Vaughan*, 1991; *Vaughan and Doake*, 1996; *Rott et al.*, 1996; *Rack and Rott*, 2004] leading to concern over the fate of the remaining ice shelves with continued warming [*Scambos et al.*, 2000] as well as an ongoing discussion of breakup mechanisms [e.g., *Scambos et al.*, 2000; 2009; *MacAyeal et al.*, 2003; *Shepherd et al.*, 2003; *Glasser and Scambos*, 2008; *Vieli et al.*, 2006]. As a contribution to assessing the role of ocean-ice interactions to the evolution of ice shelves, we have inverted the free air gravity anomalies over the Larsen C ice shelf (Figure 32) to determine the shelf bathymetry (Figure 33) and the geometry of the water-filled cavity (Figure 34) beneath the ice shelf [*Cochran et al.*, 2010; *Cochran and Bell*, submitted].

The OIB airborne data are supplemented by shipboard survey data in the former Larsen A and Larsen B areas and on the continental shelf to the east. Figure 32 shows OIB data over the ice shelf and upward continued marine gravity data over the adjacent continental shelf. The marine data is useful for a number of purposes. Inclusion of upward continued gravity in the inversion provides a means to assess the inversion since we already know the bathymetry in that region from shipboard surveys. Also, the shipboard surveys can provide independent information on geologic controls and the appropriate density contrast to use in the inversion. For example, shipboard seismic reflection data shows that the free-air gravity high running along the edge of the ice shelf at 59°W-60°W (Figure 32) does not result from seafloor morphology, but from a buried high-density ridge of crystalline rock [*Sloan et al.*, 1995]. That area was therefore excluded from the inversion (Figure 33).

The inversion utilized the well-established Parker-Oldenburg technique [*Parker*, 1973; *Oldenburg*, 1974]. The free parameters in the inversion are the density contrast across the interface and the average depth of the interface below the measurement level. We utilized the marine bathymetry data to estimate the mean depth on the continental shelf which we took to be 535 m (1050 m below the average flight height) and seismic velocity determinations from a BAS seismic refraction line on the ice shelf [*Jarvis and King*, 1995] to constrain the density contrast which we took to be 1.67 g/cm^3 (rock density = 2.7 g/cm^3 and water density = 1.03 g/cm^3).
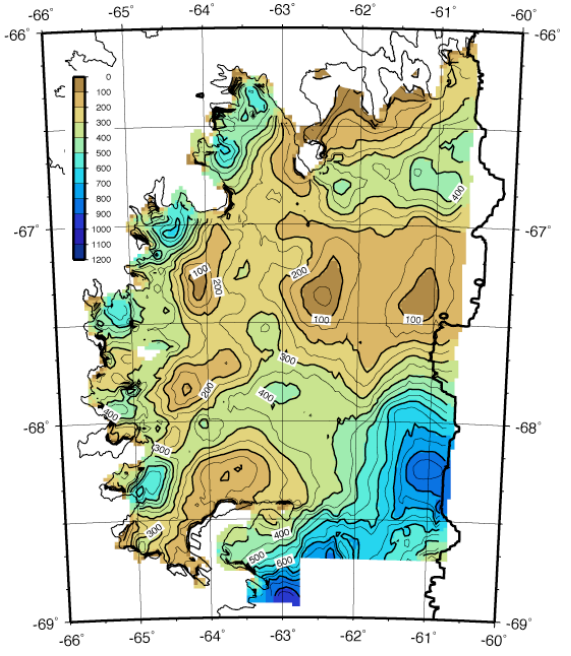
29
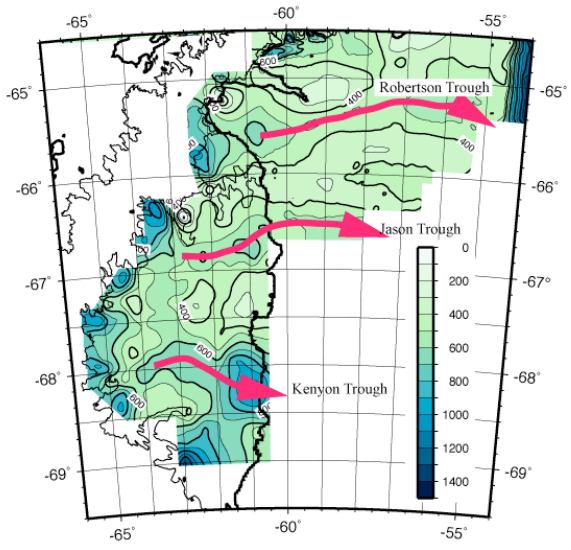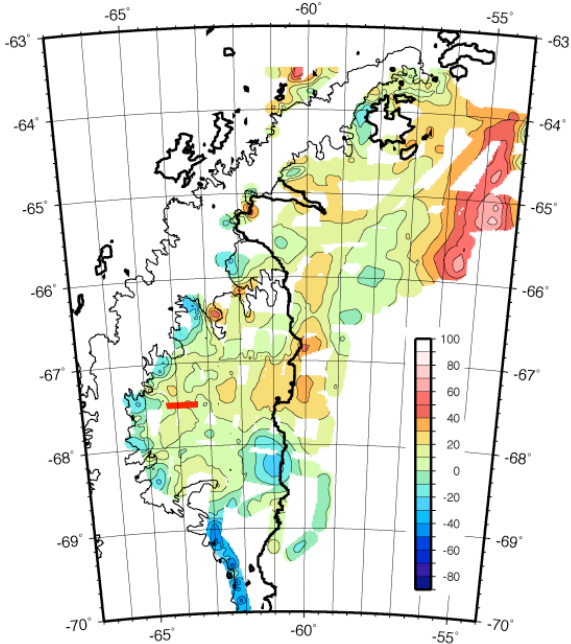
Figure 32 (above left). Free-air gravity anomaly map of the Larsen ice shelf and adjoining continental shelf contoured at 10 mGal intervals. Map is based on IceBridge airborne gravity data and shipboard data upward continued to the altitude of the flight lines. Heavy red line near 67.5°S, 64°W shows the location of a BAS seismic refraction line [*Jarvis and King*, 1995]. Figure from *Cochran and Bell* [submitted].

Figure 33 (above right). Bathymetry beneath the Larsen ice shelf determined from inversion of airborne gravity data and from shipboard measurements on the adjacent continental shelf from contoured at 100 m intervals. Red arrows show the location of broad glacial troughs across the continental shelf. *Cochran and Bell* [submitted].

Figure 34. Thickness of the water cavity beneath the Larsen ice shelf contoured at 50 m intervals. The cavity thickness is the difference between the seafloor depth determined from our inversion and the ice draft determined by *Holland et al.* [2009]. Figure from *Cochran and Bell* [submitted].

Figure 35. Changes in bathymetry beneath the Larsen ice shelf resulting from a change in the assumed bed density from 2.70 g/cm^3 to 2.60 g/cm^3. Contour interval is 5 m and 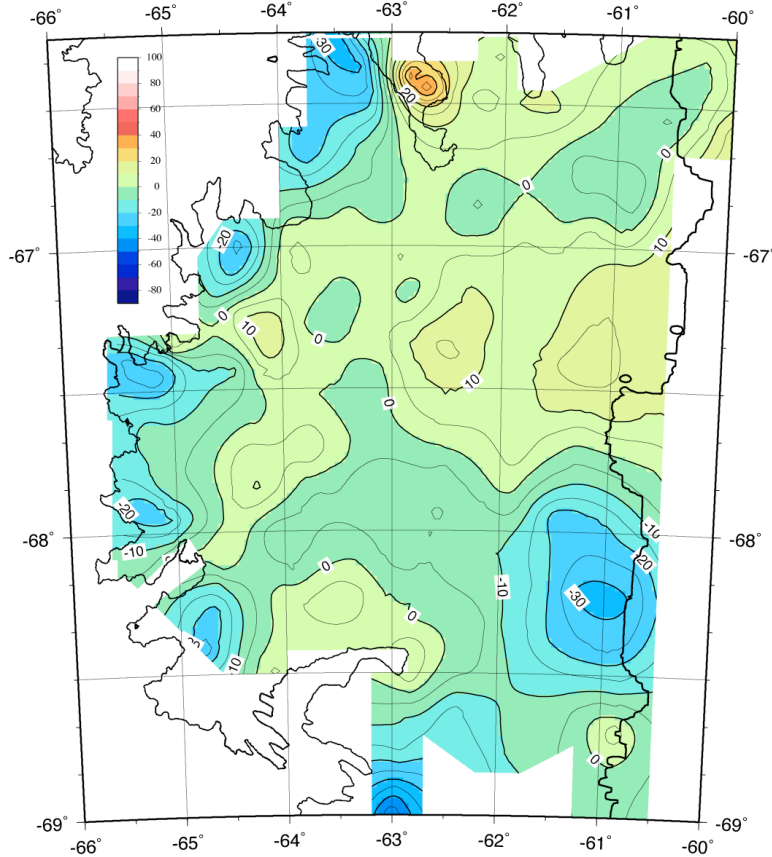color changes are at 10 m intervals. Sign convention is that positive areas have become shallower and negative areas have become deeper. Maximum changes are about ±35 m.

The results of the inversion for bathymetric relief beneath the Larsen ice shelf are shown in Figure 33 along with the shipboard bathymetry to the north and east of the airborne survey. The depth of the continental shelf determined from our inversion ranges from less than 300 m to more than 1000 m. The main features are a series of overdeepenings reaching 1000 m along the grounding lines of major glaciers and three broad troughs across the shelf (Figure 33). The thickness of the water-filled cavity determined from our bathymetry and the *Holland et al.* [2009] ice draft grid are shown in Figure 34.

There are two areas where the results of the inversion can be tested against known bathymetric depths. The inversion results over the former Larsen B area can be compared to the marine bathymetry. The depths determined from the inversion vary from about 20 m too shallow to about 45 m too deep. The second location is the *Jarvis and King* [1995] seismic refraction line. Sampling our bathymetry grid along their refraction line shows a gradient in depth from 500 m to 587 m, with a mean depth of 546 m. The *Bamber et al.* [2009b; a] Antarctic DEM gives an elevation of 54 m for the surface of the ice sheet along the refraction line. Our predicted depth of the seafloor is thus 554 to 641 m below the surface of the ice with a mean depth of 600 m below the ice surface. This is 17 m shallower than the depth determined from the seismic refraction experiment.

As discussed above, the free parameters in the inversion are the average depth and the bed density. We tested the sensitivity of the solution to variations in these parameters by redoing the inversion with different values. Figure 35 shows the depth differences when a density of 2.6 g/cm^3 rather than 2.7 g/cm^3 is assumed. In that figure, positive values mean that the bathymetry using a density of 2.6 g/cm^3 is shallower and negative values mean that the area is deeper. The shape of the contours in the difference map (Figure 35) is very similar to those on the depth map (Figure 33). This is because, with the reduced density contrast, areas shallower than the mean depth need additional mass to match the observed gravity, while areas deeper than the mean depth need a greater mass deficiency. Thus shallow areas become shallower and deep areas become deeper. If we had increased, rather than decreased the density, the opposite would have occurred. The largest depth changes are about ±30-35 m. However changes that large are confined to the very deepest and very shallowest regions. Throughout most of the area, which is within a few hundred meters of the mean depth, depth changes due to a 0.1 g/cm^3 variation in density are less than10-15 m.

We also investigated the effect of changing the mean depth, which is the other free parameter, by redoing the inversion assuming a mean depth of 460 m (975 m below the average flight height) or 75 m less than in the original inversion. This basically resulted in a DC shift of 75 m in the derived depths. Depths at all points were shallower by 69.2 to 79.9 m than in the original inversion with shallow areas at the low end and deeper areas at the higher end of that range.

Bathymetry beneath individual glaciers

Determining the bathymetry beneath individual glaciers is a very different problem than for floating ice shelves and calls for a different set of techniques. This is due both to the different scale of the feature being investigated and that the area of interest extends onshore where the ice is not floating and thus its mass must be explicitly included. (Floating ice displaces its mass of water and thus does not need to be included in calculations). We have found that a formal inversion, such as discussed above, is not the best way to proceed. It has proved much more fruitful to undertake forward modeling of individual lines, using radar data over grounded areas and any bathymetric information available seaward of the glacier as tie points to constrain the modeling. The fact that IceBridge collects ATM topography and MCoRDS radar data coincident with the gravity data is essential for the modeling.

In Antarctica, OIB has carried out grid surveys extending well beyond the grounding line of Pine Island and Thwaites glaciers, as well as the small Dotson ice shelf and the Kohler Glacier that feeds it. A survey is planned of the Crossan ice shelf and Smith Glacier. In Greenland, grid surveys of the large glaciers have tended to concentrate on the upstream, grounded portion of the glacier. However, lines have been flown down numerous glaciers along flow lines across the grounding line and along the floating tongue into open water.

We have undertaken a study of the sub-ice bathymetry at Thwaites Glacier [*Tinto et al.*, 2010; *Tinto and Bell*, submitted]. Sub-ice relief, as it was understood prior to our study [*Vaughan et al.*, 2006; *Holt et al.*, 2006; *Nitsche et al.*, 2007; *Jenkins et al.*, 2010], is shown in Figure 36a and IceBridge free-air anomalies are shown in Figure 36b. Observed gravity anomaly (Figure 36b) ranges between -53 and 13 mGal. The largest
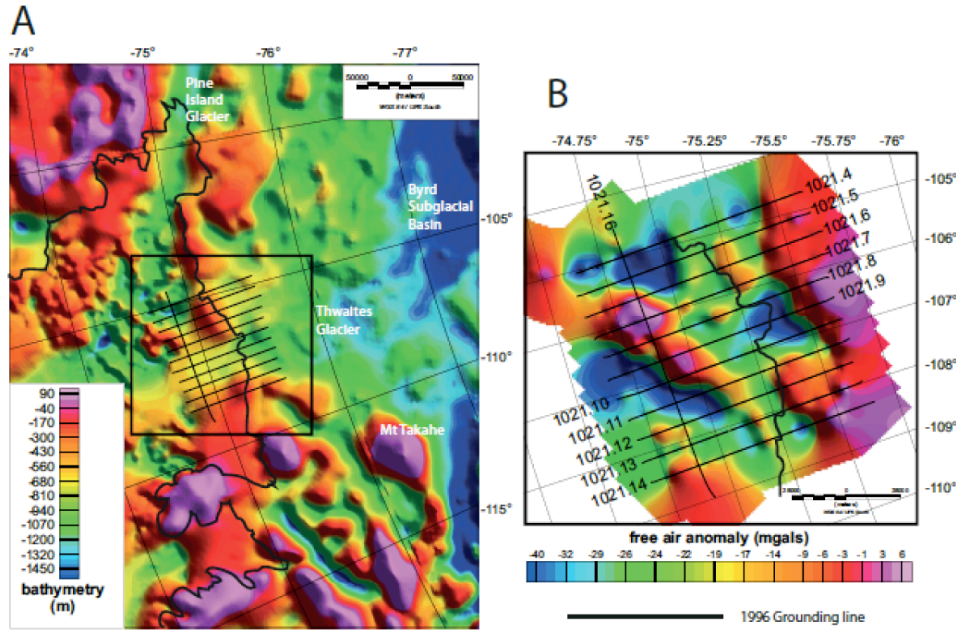
Figure 36. Maps of the survey region at the mouth of Thwaites Glacier and surroundings. A) Bathymetry from *Nitsche et al.* [2007], *Jenkins et al.* [2010] and the AGASEA survey [*Vaughan et al.*, 2006; *Holt et al.*, 2006] with IceBridge 2009 Thwaites Glacier survey lines superimposed. B) Grid of free air gravity anomaly from the IceBridge 2009 Thwaites Glacier survey. Figure from *Tinto and Bel*l [submitted].

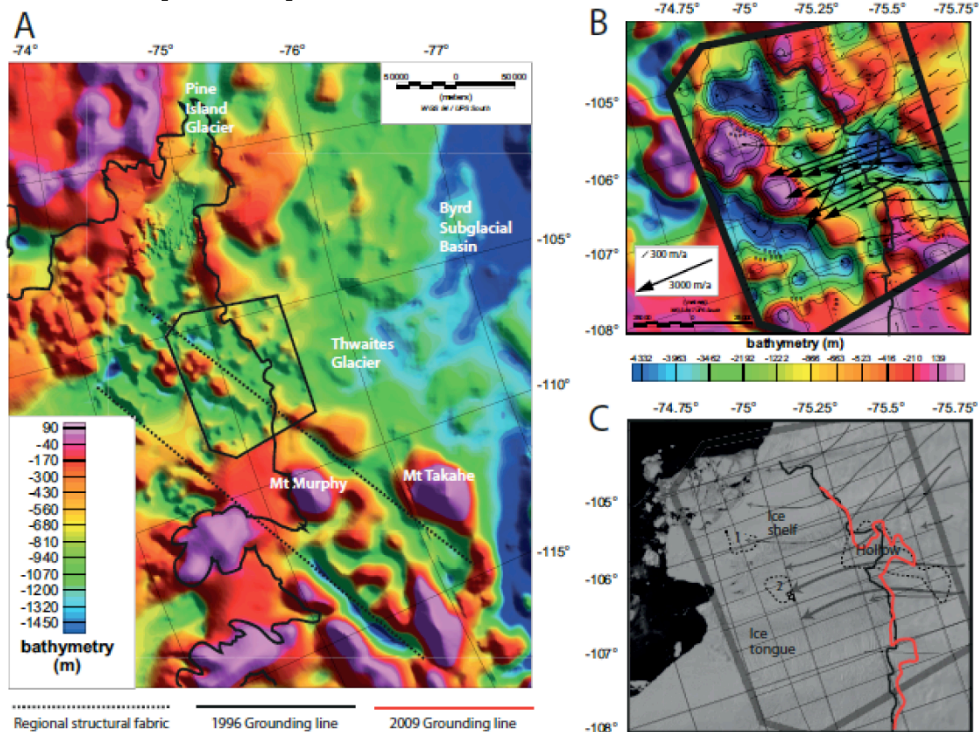*Figure 37.* Bathymetry model for Thwaites Glacier from IceBridge data. A) The regional context of the new bathymetry; B) with flow vectors from *Rignot* [2001] superimposed; C) Key features of the bathymetric model and flow regime, superimposed on a MODIS image from the day of the survey flight. Ridge is defined by 800 m depth contour and hollows are defined by 1000 m depth contour. Figure from *Tinto and Bel*l [submitted].
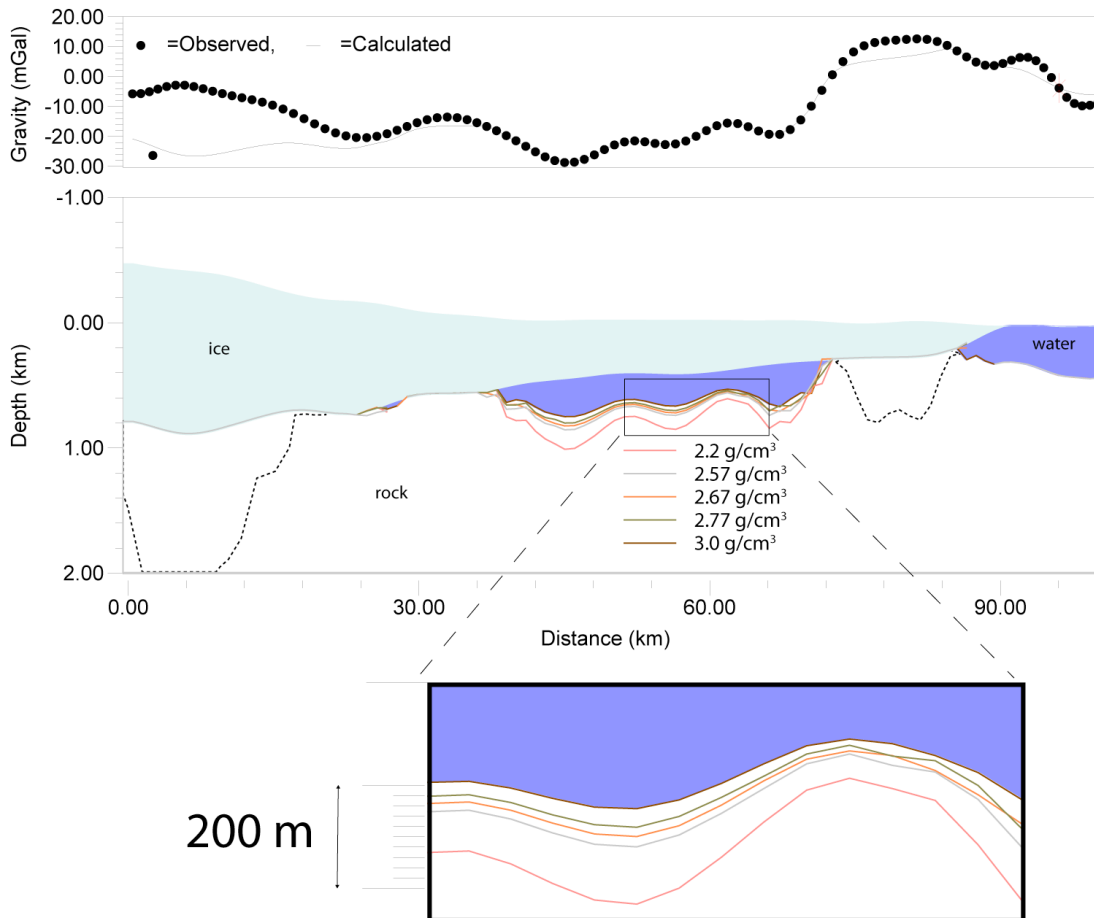
33

Figure 38. Bathymetric model along line 1021.7. Bathymetry within the water cavity beneath Thwaites is shown for a range of assumed rock densities. The calculated gravity curve is for our preferred density of 2.67 g/cm^3. Dotted lines show regions in which zones of higher density rock are required to match the observed gravity (shown for the 2.67 g/cm case).

anomaly is an elongate gravity high with values of -16 to 13 mGal, ~ 40 km offshore from the present day grounding line. A second high, ranging from -10 to 10 mGal, exists onshore of the grounding line, at the southernmost end of the survey lines.

The gravity was modeled on a line-by-line basis with constraints provided by the depth to the base of the ice measured by MCoRDS on the same line in areas of grounded ice and by known bathymetry in Pine Island Bay seaward of the ice. The rock density (2.67 g/cm^3) was chosen to be compatible with rocks exposed locally, which are granodiorites and gneisses.

Figure 38 uses line 1021.7 (see Figure 36 for location) to examine the effects of variations in the assumed bed density on the deduced bathymetry. The figure shows the bed relief deduced for a range of basement densities ranging from 2.20 to 3.00 g/cm^3. For reasonably small (0.1 g/cm^3) variations from our preferred density of 2.67 g/cm^3, the changes to the deduced bathymetry are small (of the order of 10-15 m). However, the variations in depth over the entire range of densities investigated approach 200 m. In particular, as the rock density becomes lower and the density contrast with water is significantly reduced, the changes in depth necessary to reproduce gravity variations quickly grows larger leading to much greater relief hills and valleys.

Figure 38 also illustrates another apparent source of uncertainty in the gravity modeling that actually allows us to obtain information on bed geology. The model is constrained over much of the profile by the observed ice thickness from MCoRDS data and by marine bathymetry data seaward of the ice. There are two areas along the profile (km 0-18 and km 72-82) where these constraints prevent the model from matching the observed gravity. Using a single bed density would require that the bed in these regions extend up into what is known to be ice. In these cases, denser volcanic rock was assumed to be present. These zones are shown by the dotted lines in Figure 38 for our preferred bed density of 2.67 g/cm^3. Two observations tend to support this solution. First, at the western end of the profile, a nearly 20-mGal gravity high is located over a depression in the bed, suggesting the presence of higher density rocks at that location. The second observation is that these higher density zones are required on all of the profiles and form coherent, linear zones across the survey. The trend of these zones of denser rock across the survey is consistent with the presence of dike intrusion zones originating at Mt Murphy, a late Miocene shield volcano [*LeMasurier et al.*, 1994; *Wilch and McIntosh*, 2002] located about 50 km to the west. It is thus possible, where there are adequate constraints on bed relief, to utilize the airborne gravity data to extract information on the geology of the underlying rocks.

Conclusions

1) Uncertainty in OIB gravity measurements, as determined from repeat flights is about 0.5 mGal.

2) All airborne gravity data is susceptible to crossover mismatches resulting from directional filtering. These mismatches are related to the length of the filter, the local relief in the gravity field and the geometry of the tracks. They must be considered in data interpretation, but are not a measure of instrument performance

3) Inversions and forward modeling are capable of producing bathymetry beneath ice shelf and floating ice that is accurate to within ~ ±30 m. The quality of the models is optimized when other data is available to provide ground truth on densities and to constrain water depth at places within the modeled area.

References Cited

Argyle, M., S. Ferguson, L. Sander, and S. Sander (2000), AIRGrav results: A comparison of airborne gravity data with GSC test site data, *The Leading Edge*, *19*, 1134-1138.

Bamber, J. L., J. L. Gomez-Dans, and J. A. Griggs (2009a), A New 1 km Digital Elevation Model of the Antarctic Derived from Combined Satellite Radar and Laser Data Part 1: Data and Methods., *The Cryosphere*, *3*, 101-111.

Bamber, J. L., J. L. Gomez-Dans, and J. A. Griggs (2009b), Antarctic 1 km Digital Elevation Model (DEM) from Combined ERS-1 Radar and ICESat Laser Satellite Altimetry, *National Snow and Ice Data Center, Boulder CO., Digital media.*, http://nsidc.org/data/docs/daac/nsidc0422_antarctic_0421km_dem.

Block, A. E., and R. E. Bell (submitted), Geophysical evidence for soft bed sliding at Jakobshavn Isbrae, West Greenland, *J. Geophys. Res.*

Briggs, I. C. (1974), Machine contouring using minimum curvature, *Geophysics*, *39*, 39-48. doi:10.1190/1.1440410.

Cochran, J. R., R. E. Bell, N. Frearson, and S. Elieff (2010), Inversion of IceBridge gravity data for continental shelf bathymetry beneath the Larsen ice shelf., *Eos. Trans. AGU Fall meeting Suppl.*, *91*, Abstract C14A-05.

Cochran, J. R., and R. E. Bell (submitted), Inversion of IceBridge gravity data for continental shelf bathymetry beneath the Larsen ice shelf, *J. Glaciology*.

Doake, C. S. M., and D. G. Vaughan (1991), Rapid disintegration of the Wordie ice shelf in response to atmospheric warming, *Nature*, *350*, 328-330.

Ferguson, S. (2010), Investigation of the Capability of Sander Geophysics' AIRGrav System for Geodetic Purposes: Condensed Summary, *Sander Geophysical Limited Technical Report*, 20p.

Glasser, N. F., and T. A. Scambos (2008), A structural glaciological analysis of the 2002 Larsen B ice shelf collapse, *J. Glaciology*, *54*, 3-16.

Holland, D. M., H. F. J. Corr, D. G. Vaughan, A. Jenkins, and P. Skvarca (2009), Marine ice in Larsen ice shelf, *Geophys. Res. Lett.*, *36*, L11604. doi:10.1029/2009GL038162.

Holt, J. W., D. D. Blankenship, D. L. Morse, D. A. Young, M. E. Peters, S. D. Kempf, T. G. Richter, D. G. Vaughan, and H. F. J. Corr (2006), New boundary conditions for the West Antarctic Ice Sheet: Subglacial topography of the Thwaites and Smith glacier catchments, *Geophys. Res. Lett.*, *33*, L09502, doi:01029/02005GL025561.

Jarvis, E. P., and E. C. King (1995), Seismic investigation of the Larsen Ice Shelf, Antarctica: in search of the Larsen Basin, *Antarctic Science*, *7*, 181-190.

Jenkins, A., P. Dutrieux, S. S. Jacobs, S. D. McPhail, J. R. Perett, A. T. Webb, and D. White (2010), Observations beneath Pine Island Glacier in West Antarctica and implications for its retreat, *Nature Geoscience*, *3*, 468-472. doi:10.1038/NGE0890.

LeMasurier, W. E., D. M. Harwod, and D. C. Rex (1994), Geology of Mount Murphy Volcano: An 8-m.y. history of interaction between a rift volcano and the West Antarctic ice sheet, *Bull. Geol. Soc. Am.*, *106*, 265-280.

MacAyeal, D. R., T. A. Scambos, C. L. Hulbe, and M. A. Fahnestock (2003), Catastrophic ice-shelf break-up by an ice-shelf-fragment-capsize mechanism, *J. Glaciology*, *49*, 22-36.

Nitsche, R. O., S. S. Jacobs, L. R.D., and K. Gohl (2007), Bathymetry of the Amundsen Sea continental shelf: Implications for geology, oceanography and glaciology, *Geochem. Geophys. Geosyst.*, *8*(10), Q10009, doi:10010.11029/12007GC001694.

Oldenburg, D. W. (1974), The inversion and interpretation of gravity anomalies, *Geophysics*, *39*, 536-536.

Parker, R. L. (1973), The rapid calculation of potential anomalies, *Geophys. J. R. Astron. Soc.*, *31*, 447-455.

Rack, W., and H. Rott (2004), Pattern of retreat and disintegration of the Larsen B ice shelf, Antarctic Peninsula, *Ann. Glaciology*, *39*, 505-510.

Rignot, E. (2001), Evidence for rapid retreat and mass loss of Thwaites Glacier, West Antarctica, *J. Glaciology*, *47*, 213-222.

Rott, H., P. Skvarca, and T. Nagler (1996), Rapid collapse of the northern Larsen ice shelf, Antarctica, *Science*, *271*, 788-792.

Sander, S., M. Argyle, S. Elieff, S. Ferguson, V. Lavoie, and L. Sander (2004), The AIRGrav aiborne gravity system, in *Airborne Gravity 2004 - Australian Society of Exploration Geophysicists Workshop*, edited by R. Lane, pp. 49-53, Geoscience Australia, http://www.ga.gov.au/image_cache/GA16642.pdf.

Scambos, T. A., C. L. Hulbe, M. A. Fahnestock, and J. Bohlander (2000), The link between climate warming and the break-up of ice shelves in the Antarctic Peninsula, *J. Glaciology*, *46*, 516-530.

Scambos, T. A., H. A. Fricker, C. C. Liu, J. Bohlander, J. Fastook, A. Sargent, R. Massom, and A. M. Wu (2009), Ice shelf disintegration by plate bending and hydro-fracture: Satellite observations and model results of the 2008 Wilkins ice shelf break-ups, *Earth Planet. Sci. Lett,*, *280*, 51-60. doi:10.1016/j.epsl.2008.12.027.

Shepherd, A., D. Wingham, A. J. Payne, and P. Skvarca (2003), Larsen ice shelf has progressively thinned, *Science*, *302*, 856-859. doi:10.1126/science.1089768.

Sloan, B. J., L. A. Lawver, and J. B. Anderson (1995), Seismic stratigraphy of the Larsen Basin, Eastern Antarctic Peninsula, in *Geology and Seismic Stratigraphy of the Antarctic Margin*, edited by A. K. Cooper, P. F. Barker and G. Brancolini, pp. 59-74, Antarctic Research Series. v 68, American Geophysical Union

Studinger, M., R. E. Bell, and N. Frearson (2007), Gravimeter test flights to the North Pole, paper presented at 10th International Symposium on Antarctic Earth Sciences, Santa Barbara, CA, Aug. 26 - Sept. 1, 2007.

Studinger, M., R. E. Bell, and N. Frearson (2008), Comparison of AIRGrav and GT-1A airborne gravimeters for research applications, *Geophysics*, *73*, 151-161.

Tinto, K. J., R. E. Bell, J. R. Cochran, S. Elieff, and N. Frearson (2010), Insights into the Thwaites Glacier grounding zone from Operation IceBridge aerogravity, *Eos. Trans. AGU Fall meeting Suppl.*, *91*, Abstract C11A-0529.

Tinto, K. J., and R. E. Bell (submitted), Progressive unpinning of Thwaites Glacier from newly identified offshore ridge - constraints from aerogravity, *Geophys. Res. Lett.*

Vaughan, D. G., and C. S. M. Doake (1996), Recent atmospheric warming and retreat of ice shelves on the Antarctic Peninsula, *Nature*, *379*, 328-331.

Vaughan, D. G., H. F. J. Corr, F. Ferraccioli, N. Frearson, A. O'Hare, D. Mach, J. W. Holt, D. D. Blankenship, D. L. Morse, and D. A. Young (2006), New boundary conditions for the West Antarctic ice sheet: Subglacial topography beneath Pine Island Glacier, *Geophys. Res. Lett.*, *33*, L09501, doi:09510.01029/02005GL025588.

Vieli, A., A. J. Payne, Z. Du, and A. Shepherd (2006), Numerical modelling and data assimilation of the Larsen B ice shelf, Antarctic Peninsula, *Phil. Trans. R. Soc. London*, *364*, 1815-1839. doi:10.1098/rsta.2006.1800.

Wilch, T. I., and W. C. McIntosh (2002), Lithofacies analysis and ^{40}Ar/^{39}Ar geochronology of ice-volcano interactions at Mt.Murphy and the Crary Mountains, Marie Byrd Lan, Antarctica, in *Volcano-Ice Interactions on Earth and Mars*, edited by J. L. Smellie and M. G. Chapman, pp. 237-253, Geological Society of London Special Publication 202